Marine Geophysical Research (2026) 47:10
https://doi.org/10.1007/s11001-026-09608-8

ORIGINAL RESEARCH PAPER

# Quantitative fluid discrimination through AVO/EEI analysis and semi-supervised machine learning method: a case study from the Bahregansar field, Ghar sandstone reservoir

**Hessam Mansouri Siahgoli**[1] · **Mohammad Ali Riahi**[1] · **Majid Nabi-Bidhendi**[1] · **Mohammad Emami Niri**[2]

Received: 22 September 2025 / Accepted: 5 January 2026


## Abstract

This study presents an integrated approach for quantitative fluid discrimination in the Ghar sandstone reservoir through the combined application of amplitude versus offset (AVO) analysis, Extended Elastic Impedance (EEI) inversion, and semi-supervised Probabilistic Neural Network (PNN) machine learning techniques. The methodology addresses critical challenges in hydrocarbon detection within complex reservoir environments where conventional seismic interpretation methods prove insufficient. The theoretical framework encompasses comprehensive AVO attribute generation utilizing Zoeppritz equation approximations, including intercept, gradient, AVO product, fluid factor, gas indicator, and Poisson's Ratio Contrast attributes. Extended Elastic Impedance analysis was systematically applied across eight wells to determine optimal chi angles through cross-correlation analysis, identifying a consistent optimal chi angle of 32° for water saturation discrimination. The EEI methodology enables enhanced sensitivity to fluid variations through angle-dependent projections of elastic properties, addressing limitations in conventional elastic impedance approaches. Pre-stack simultaneous seismic inversion generated high-resolution P-impedance, S-impedance, and density volumes, providing foundation for comprehensive AVO attribute extraction and EEI analysis. Integration of multiple seismic attributes through EEI attribute volume generation enabled spatial extrapolation of reservoir property relationships from well locations to the complete survey area. The final stage employed semi-supervised PNN analysis utilizing EEI and AVO attribute maps as input parameters for training and prediction of oil, gas, and water distribution. Results demonstrate successful fluid discrimination with gas accumulations concentrated in structural crests, oil presence along southern flanks, and water distribution throughout broader reservoir intervals. Gas discrimination predictions were fully validated against production data and gas-oil contact surface, while oil distribution results can be verified using gas–oil and oil–water contact surfaces (GOC and OWC). However, water distribution probability maps remain unverified due to the absence of available well data for validation. The integrated approach provides a robust framework for reducing exploration risks and optimizing field development strategies in complex reservoir environments, demonstrating enhanced fluid discrimination capabilities through advanced seismic analysis techniques.

**Keywords** AVO analysis · Extended elastic impedance · Probabilistic neural network · Fluid discrimination · Ghar sandstone

✉ Mohammad Ali Riahi
mariahi@ut.ac.ir

[1] Institute of Geophysics, University of Tehran, Tehran, Iran

[2] Institute of Petroleum Engineering, School of Chemical Engineering, College of Engineering University of Tehran, Tehran, Iran

### Abbreviations

| | |
|---|---|
| AVO | Amplitude versus offset |
| EEI | Extended elastic impedance |
| PNN | Probabilistic neural network |
| ANN | Artificial Neural Network |
| CNN | Convolutional neural network |
| PDF | Probability density function |
| SOM | Self-organizing map |
| PRC | Poisson's ratio contrast |

Published online: 29 January 2026

| | |
|---|---|
| LMR | Lambda-Mu-Rho |
| MARS | Multi-attribute rotation scheme |
| CPEI | Curved pseudo-elastic impedance |
| HQGA | Hybrid quantum genetic algorithm |
| ZFTB | Zagros fold-and-thrust belt |
| VTI | Vertical transverse isotropy |
| RPT | Rock physics template |
| DHI | Direct hydrocarbon indicators |
| ML | Machine learning |
| UVQ | Unsupervised vector quantization |
| PCA | Principal component analysis |
| TFL | Thinned Fault Likelihood |
| WDDM | West Delta Deep Marine |
| MLFN | Multilayer feedforward network |
| MSE | Mean squared error |
| SGD | Stochastic gradient descent |

## Introduction

The quantitative discrimination of fluid types in reservoir characterization represents a fundamental challenge in hydrocarbon exploration, requiring sophisticated integration of geophysical and computational methodologies. These challenges stem primarily from the inherent resolution limitations of seismic data relative to reservoir-scale heterogeneities, non-uniqueness in geophysical responses where different lithology-porosity-fluid combinations produce similar signatures, and scale mismatches between point-source well measurements and continuous seismic coverage, compounded by data quality issues and anisotropic effects that can mask or mimic fluid responses. The evolution from traditional bright spot analysis to advanced amplitude versus offset (AVO) techniques has significantly enhanced the ability to detect hydrocarbon accumulations, particularly in complex geological settings where conventional methods prove inadequate. The development of extended elastic impedance (EEI) inversion has further revolutionized this field by providing enhanced sensitivity to fluid variations through optimal angle-dependent projections of elastic properties, while the integration of machine learning approaches offers new possibilities for pattern recognition in complex reservoir environments.

### Traditional AVO and elastic impedance methodologies

The theoretical foundation for modern AVO analysis emerged from Bortfeld's (1961) practical approximations to the Zoeppritz equations for calculating P- and S-wave reflection coefficients (Fawad et al. 2020). Aki and Richards (1981) introduced linearization approaches for quantitative interpretation, subsequently simplified by Shuey (1985) for density extraction from wide-angle AVO data (Aki and Richards 1981). Ostrander (1984) demonstrated that gas-saturated sands exhibit distinctive Poisson's ratio characteristics compared to brine-saturated formations, establishing the foundation for systematic AVO-based fluid discrimination (Ostrander 1984). Rutherford and Williams (1989) developed a systematic AVO anomaly classification based on zero-angle reflection coefficients, later expanded by Castagna and Swan (1997) to include Class IV anomalies (Rutherford and Williams 1989; Castagna and Swan 1997). Recognizing that standard AVO attributes could not effectively isolate fluid effects from lithological variations, Smith and Gidlow (1987) introduced weighted stack concepts for generating difference stacks relative to wet background trends (Smith and Gidlow 1987). To address ambiguities in fluid discrimination using conventional intercept-gradient analysis alone, Verm and Hilterman (1995) developed normal incidence and Poisson reflectivity parameters, enabling improved discrimination of fluid-bearing lithologies through colour-coded matrix analysis (Verm and Hilterman 1995). Goodway et al. (1997) introduced the Lambda-Mu-Rho (LMR) methodology utilizing Lamé parameters for enhanced fluid sensitivity (Goodway et al. 1997). Lambda ($\lambda$) demonstrates superior correlation with bulk modulus variations and fluid content, mu ($\mu$) enables lithology discrimination independent of fluid effects through its sensitivity to rock rigidity, while rho ($\rho$) represents bulk density providing additional constraints on both lithology and fluid properties (Goodway et al. 1997). Addressing the limitation that conventional AVO attributes are tied to specific angles and may not optimize sensitivity for all reservoir types, Connolly (1999) introduced elastic impedance, extended to Extended Elastic Impedance (EEI) by Whitcombe et al. (2002b), which eliminates dimensionality dependence through normalization with reference constants and allows rotation of elastic property space to any angle for optimization of specific target properties (Connolly 1999; Whitcombe 2002a, 2002b; Aleardi 2018; Fawad et al. 2020). Early inversion methods were developed by Delas et al. (1970), Lindseth (1972), and Lavergne (1975) for processing seismic data to increase geological information availability (Fawad et al. 2020). Ma (2002) combined AVO extraction and impedance inversion using simulated annealing, while Hampson et al. (2005) modified formulations using small reflectivity approximations (Ma 2002; Hampson et al. 2005). The stability of simultaneous inversion is enhanced through background models capturing P-impedance relationships, though this presents challenges with varying Vp/Vs ratios across different lithologies, as significant variations (e.g., sandstone ~ 1.7, shale ~ 2.0–3.0) create ill-conditioned inversion matrices and increase parameter trade-offs, necessitating stabilization constraints (Mansouri Siahgoli et al. 2025). Recent developments include inverse rock physics modeling for direct quantitative prediction of lithology and reservoir quality (Johansen et al. 2004), Curved Pseudo-elastic Impedance (CPEI) mimicking EEI using acoustic impedance and Vp/Vs (Fawad et al. 2020), and multi-attribute rotation scheme (MARS) by Alvarez et al. (2015) for predicting petrophysical properties from elastic attributes. Contemporary applications in hydrocarbon reservoirs have demonstrated the effectiveness of integrating multiple seismic attributes with AVO analysis for enhanced fluid characterization. Farfour and Foster (2022) successfully applied this integrated approach in the Poseidon field, offshore northwest Australia, combining AVO attributes with acoustic impedance, Vp/Vs ratio, and lambda-rho to discriminate hydrocarbon-saturated reservoirs in challenging geological settings, demonstrating improved fluid detection reliability through multi-attribute analysis compared to conventional single-attribute interpretation (Farfour and Foster 2022).

## Advanced computational and machine learning approaches

Nonlinear optimization methods, including genetic algorithms and quantum-inspired approaches, address limitations of linear AVO inversion in complex environments by working directly with exact Zoeppritz equations rather than linearized approximations, enabling more accurate parameter estimation in reservoirs with strong impedance contrasts and avoiding the weak-contrast assumptions inherent to traditional methods. The hybrid quantum genetic algorithm (HQGA) leverages quantum superposition principles to explore solution space more efficiently than conventional genetic algorithms, achieving faster convergence and more robust global optimization for elastic parameter estimation through parallel evaluation of multiple solution paths (Cheng et al. 2022). Machine learning integration represents the current frontier, with unsupervised neural networks demonstrating promise in fluid facies classification (Qian et al. 2018; Russell and Hedlin 2019). Deep learning approaches, including CNNs, show superior performance in seismic facies classification and fluid prediction (Zhang et al. 2014; Araya-Polo et al. 2018). The integration of Bayesian classification methods with artificial neural networks addresses traditional method limitations (Mansouri Siahgoli et al. 2025), combining the uncertainty quantification capabilities of Bayesian frameworks with the nonlinear pattern recognition strengths of ANNs to provide probabilistic predictions that incorporate both prior geological knowledge and data-driven learning, while also handling sparse data through regularization that prevents overfitting (Feng 2020; Narayan et al. 2023). The successful implementation of quantitative fluid discrimination requires integrating multiple analytical approaches, combining AVO/EEI sensitivity with machine learning pattern recognition capabilities. Semi-supervised learning and probabilistic neural network (PNN) methodologies provide frameworks for handling uncertainty while maintaining computational efficiency, with semi-supervised approaches particularly valuable for leveraging abundant unlabeled seismic data alongside sparse labeled well data to improve generalization and provide spatially-variant uncertainty estimates that reflect both data density and geological complexity, creating robust frameworks for reducing exploration risks in complex reservoir environments. The advancement of direct elastic parameter inversion using exact formulations has shown significant improvements over traditional approximate methods in reservoir characterization. Song et al. (2023) developed a new form of the exact Zoeppritz equation expressed in terms of Young's modulus, Poisson's ratio, and density, demonstrating superior accuracy compared to approximate equations, particularly at large incident angles (Song et al. 2023). Their iteratively regularized Levenberg–Marquardt algorithm-based inversion method proved effective for sweet spot evaluation in unconventional shale reservoirs. Similarly, marine applications have shown promising results, as demonstrated by Guangjian et al. (2023) in the Chaoshan Depression of the South China Sea, where pre-stack elastic parameter inversion successfully predicted oil and gas accumulations in Mesozoic sandstone reservoirs through comprehensive analysis of P-wave velocity, density, and Poisson's ratio characteristics, achieving effective reservoir delineation in deep-water exploration environments with limited well control (Guangjian et al. 2023).

# Workflow explanation

This workflow presents an integrated methodology for fluid discrimination in reservoir characterization that combines Extended Elastic Impedance (EEI) analysis with semi-supervised neural network techniques. The process begins with rock physics and petrophysical evaluation to establish baseline parameters, followed by EEI log analysis, where the optimal chi angle is quantitatively determined by systematically computing EEI logs across the complete angular spectrum from $-90°$ to $+90°$ and calculating Pearson correlation coefficients with water saturation logs (SWE) at each well location; cross-correlation analysis across multiple wells consistently identified $\chi = 32°$ as providing maximum correlation with water saturation, which was validated through direct visual comparison of EEI(32°) trends with SWE logs within reservoir intervals (Figs. 3 and 5). Once validated, the analysis extracts multiple AVO attributes, including Fluid Factor (FF), Gas Indicator (GI), Gradient (G), Intercept (I), and Poisson's Ratio Contrast (PRC) from pre-stack seismic data, which are then integrated with EEI attributes derived using the optimized chi angle. The final stage employs a Probabilistic Neural Network (PNN) implemented through Petrel's neural network module using a semi-supervised learning approach, where the network architecture utilizes six seismic attributes as input parameters (EEI at $\chi = 32°$, intercept, gradient, fluid factor, gas indicator, Poisson's ratio contrast) with Gaussian kernel-based pattern recognition and summation layers that generate probabilistic outputs for three fluid classes (oil, gas, water); the semi-supervised training methodology begins with labeled samples from available wells and iteratively incorporates high-confidence predictions from the unlabeled seismic volume as pseudo-labeled training data until convergence, effectively expanding the training dataset while leveraging the abundant unlabeled seismic information to improve generalization and prediction accuracy. The workflow demonstrates a systematic approach to fluid discrimination by leveraging both traditional AVO analysis and advanced machine learning techniques, ultimately generating comprehensive fluid facies maps that distinguish between water, oil, and gas distributions within the reservoir. This integrated methodology provides enhanced reliability in fluid prediction by incorporating multiple independent seismic attributes and utilizing the pattern recognition capabilities of neural networks to identify complex fluid signatures that may not be apparent through conventional analysis alone (Fig. 1).

## Geological setting

The Persian Gulf is a shallow epicontinental sea, forming a foreland depression within the Zagros Fold-and-Thrust Belt (ZFTB). The region represents one of the world's most hydrocarbon-rich areas due to abundant extensive source rocks, high-quality carbonate and sandstone reservoirs, effective regional seals, ongoing sedimentation, and significant structural traps (Konyuhov and Maleki 2006; Soleimany and Sàbat 2010; Mohammadrezaei et al. 2020).

### Tectonic evolution and structural framework of the Persian Gulf Basin

The evolution of the ZFTB and Persian Gulf has been profoundly influenced by major tectonic events involving the Arabian plate across five distinct phases: (1) Precambrian Compressional Event marked by Afro-Arabian plate assembly; (2) Upper Precambrian to Upper Devonian characterized by Paleo-Tethys subduction beneath the Gondwana margin; (3) Upper Devonian to Middle Permian defined by continental rifting and Neo-Tethys Ocean emergence; (4) Lower to Upper Cretaceous notable for Neo-Tethys subduction beneath the Eurasian plate; and (5) Miocene Era highlighted by continent-to-continent collision between Eurasian and Afro-Arabian plates. Currently, convergence persists predominantly in a north–south direction (Sharland et al. 2004; Lacombe et al. 2006; Agard et al. 2011; Mouthereau et al. 2012; Cai et al. 2021). The ZFTB is characterized by a tectonic wedge forming an asymmetrical sedimentary basin with NW–SE-oriented thrusts and folds of varying geometry and size. The belt subdivides into several regions, including the Dezful Embayment, Izeh Zone, Fars Zone, Lurestan Zone, and Abadan Plain, defined by major fault systems such as the Hendijan-Bahregansar-Nowrooz Fault (HBNF), Kazerun Fault, High Zagros Fault, Balarud Fault, and Mountain Front Fault (Pirouz et al. 2011; Mouthereau et al. 2012; Orang et al. 2018). Four primary structural trends control basement faulting: the Arabian trend (North–South and NNE-SSW), Zagros trend (NW–SE), Aulitic trend (NE-SW), and Tethyan trend (E-W). These trends govern structural features including fractures, faults, folds, tectonic subsidence, and active salt tectonism (Edgell 1996; Bahroudi and Talbot 2003; Sepehr and Cosgrove 2007). The HBNF, trending NNE-SSW, constitutes an active basement fault system with predominantly vertical orientation and dextral-reverse kinematics (Mohammadrezaei et al. 2020). This fault system created the Safaniya-Bahregansar Paleo-high, hosting numerous structural anticlinal traps including Nowruz, Bahregansar, and Hendijan in the Iranian sector, and Safaniya-Khafji, Hout, and Dora structures in the Arabian sector (Sharland et al. 2004; Ghazban 2007).

### Stratigraphy and Lithofacies characterization of the Oligocene–Miocene Ghar formation

The Oligocene–Miocene succession in the northwestern Persian Gulf comprises two distinct members: the upper siliciclastic Ghar member and the lower carbonate Asmari Limestone. These formations constitute significant hydrocarbon reservoirs throughout the region, including the Bahregansar field. The Ghar Formation type locality represents a subsurface 422-foot-thick sequence of sandstone interbedded with sandy limestone, gypseous streaks, and shale, drilled in Zubair well No. 3, southern Iraq, and assigned to Lower Miocene age based on stratigraphic considerations (Khalaf et al. 2019). The notable lithological transition from Oligocene Asmari limestone carbonate sediments to predominantly siliciclastic Ghar Sandstone reflects the second period of pivotal anti-clockwise Arabian Plate movement. Omar and Steckler (1995) documented that this second stage of tectonic activity, which initiated Red

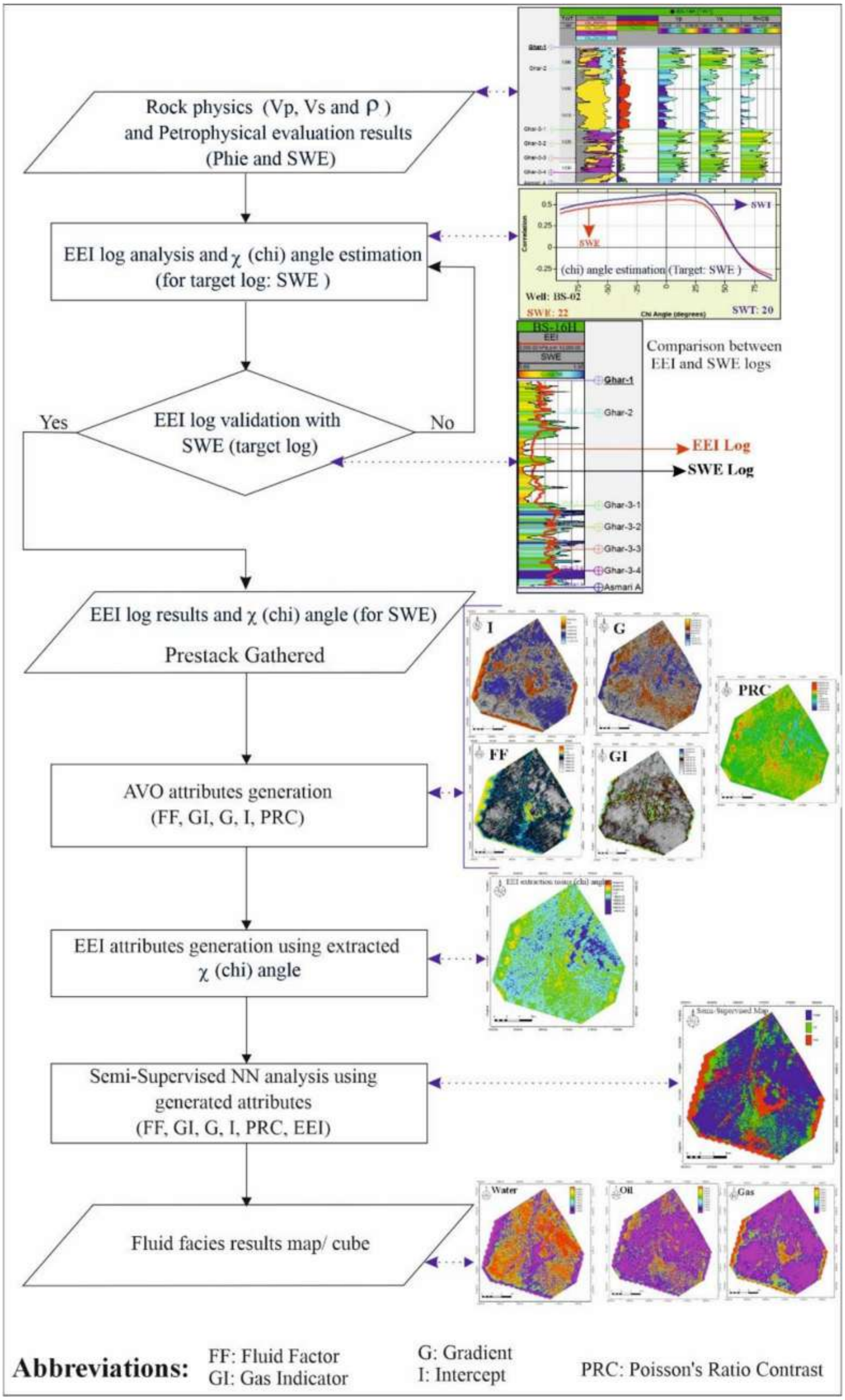


**Fig. 1** Integrated workflow for fluid discrimination combining Extended Elastic Impedance (EEI) analysis with semi-supervised neural network techniques

Sea rifting, commenced during the Late Oligocene to Early Miocene, approximately 21–25 million years ago (Omar and Steckler 1995). In the Bahregansar field, the Ghar Formation exhibits four principal lithofacies: unconsolidated sandstones, sandy limestone/dolomite, shale, and carbonate lithofacies. Petrographic analysis, geochemical investigation, and macroscopic geological observations indicate that the Ghar reservoir developed within a multifaceted fluvio-marine depositional environment encompassing shallow braided channels, interchannel floodplains, and coastal semi-closed shallow lagoons (Khalaf et al. 2019; Du et al. 2022). Lateral and vertical lithofacies variations within the Ghar sequence demonstrate cyclical sedimentation patterns indicative of intermittent climatic fluctuations. The Ghar sandstone member subdivides into two distinct units based on sandstone prevalence: Ghar-1 and Ghar-2. Ghar-1, representing the youngest sedimentary sequence, exhibits minimal sandstone content and consists primarily of carbonate and shale sediments with limited reservoir properties. Ghar-2, characterized by higher sandstone abundance, constitutes the primary gas and oil reservoir component. The upper Ghar-2 section comprises predominantly unconsolidated sandstone forming the gas reservoir, while the lower portion contains the oil reservoir with reduced sandstone proportions (Fig. 2).

## Available data set

This investigation employs a multi-disciplinary dataset from the Bahregansar field, northwestern Persian Gulf, previously validated for lithofacies classification (Mansouri Siahgoli et al. 2025). The integrated dataset provides foundation for quantitative fluid discrimination analysis within the WGS 84-UTM Zone 39 N coordinate system.

### Seismic data

The 3D seismic dataset originates from a 2006–2007 marine survey covering 313 km$^2$ of the Bahregansar structure. Seismic grid boundaries encompass 800 inlines (900–1700) and 800 crosslines (196–996) with a nominal fold of 40,

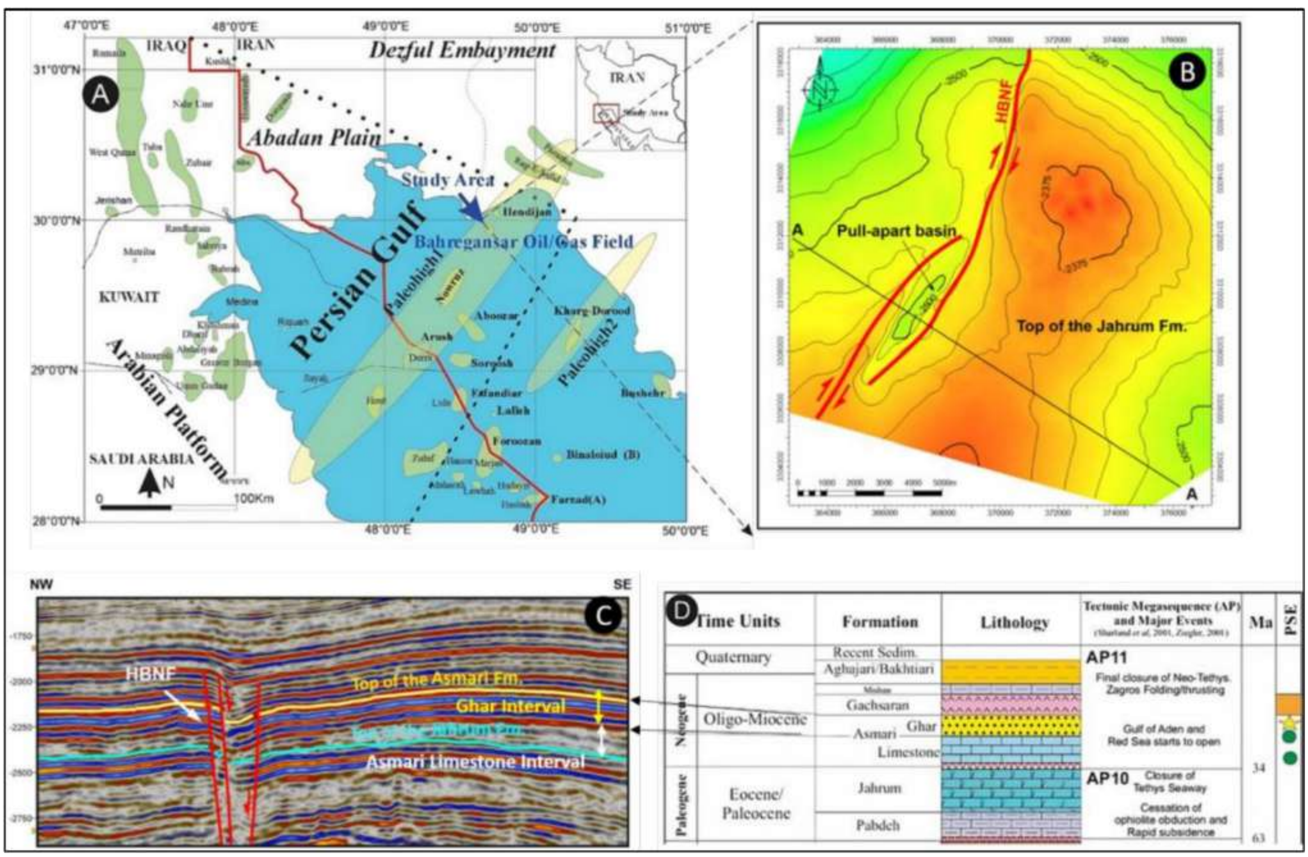


**Fig. 2** **(A)** The location of the Bahregansar field and the surrounding fields in the Iranian and Arab sectors of the Persian Gulf. The basement dextral reverse kinematics fault (HBNF) as well as the position of the Safaniya-Bahregansar paleohigh are caused by HBNF action. **(B)** The structural map derived from the top of the Upper Eocene Jahrum Formation along the Bahregansar anticline, and **(C)** Fault interpretation of the seismic section AB showing the depressed portions within the developed pull-apart basin in the Asmari and Jahrum formations and (D) Paleocene-Quaternary stratigraphic column and related tectonic megasequence in Bahregansar Field (**B** and **C** modified from Mohammadrezaei et al. 2022)

reorganized into 20 offset classes for AVO analysis. Both pre-stack and post-stack volumes underwent processing to preserve amplitude characteristics essential for Extended Elastic Impedance workflows.

### Well control and petrophysical raw data

Eight wells (BS-01, BS-02, BS-03, BS-04, BS-06, BS-07, BS-09, BS-16H) provide comprehensive subsurface control, including coordinates, geological markers, Kelly bushing elevations, and complete petrophysical log suites only in the crest section of the Bahregansar structure. Key measurements include sonic transit time (DT), bulk density (RHOB), and gamma-ray logs. The Gardner equation provided density estimates where direct measurements were unavailable, calibrated through density-velocity cross-plots.

### Petrophysical evaluated data

Petrophysical evaluations encompass quantitative mineral volumes (clay, calcite, dolomite, sandstone), water saturation calculations, effective porosity measurements, and lithofacies classifications. However, in the current study, unlike (Mansouri Siahgoli et al. 2025), water saturation and effective porosity are identified as the most important and critical parameters among the evaluated log properties.

### Seismic interpretation

Seismic horizon interpretation was conducted in the time domain across the entire Ghar Formation interval to establish a robust structural framework and geological control for the study. The seismic wavelet was extracted using a deterministic well-based methodology that leveraged reflectivity information to precisely calibrate both amplitude and phase spectral components, ensuring optimal conditions for subsequent seismic inversion procedures.

### Validation data

For validation of the results, production data from wells and fluid contact levels are required (GOC and OWC). The fluid contacts are determined based on reservoir testing data (MDT and DST) and petrophysical data, including resistivity logs. Additionally, final TDR information and velocity equations are utilized to convert fluid contact levels from depth to the time domain for validation purposes.

Table 1 Summaries of integrated dataset specifications for quantitative fluid discrimination analysis in the Bahregansar field, including 3D seismic survey parameters, well control data, petrophysical measurements, and seismic interpretation workflows with associated quality control procedures.

## Methodology

### Optimal chi angle determination for extended elastic impedance analysis

The estimation of reservoir properties through Extended Elastic Impedance log analysis requires systematic investigation of EEI log correlation characteristics at individual well locations, with water saturation logs serving as the primary target parameter for fluid discrimination analysis in the Ghar sandstone reservoir. The optimization process involves a comprehensive evaluation of correlation coefficients between EEI logs and target properties across the complete chi angle spectrum, ranging from $-90°$ to $+90°$, enabling identification of the optimal chi angle that maximizes correlation sensitivity. EEI logs at each chi angle were computed using the normalized formulation described in Sect. "EEI Analysis", where VP, VS, and ρ from sonic and density well logs are combined with reference constants (VP0, VS0, ρ0) representing average reservoir values, with systematic chi angle variation generating a complete EEI log suite for correlation analysis. The correlation analysis

**Table 1** Summary of integrated dataset specifications for quantitative fluid discrimination analysis in the Bahregansar field, including 3D seismic survey parameters, well control data, petrophysical measurements, and seismic interpretation workflows with associated quality control procedures

| No. | Data component | Specifications | Quality control |
|---|---|---|---|
| 4.1 | 3D seismic survey | 2006–2007 marine acquisition, 313 $km^2$ coverage; Grid: 800 × 800 (inlines 900–1700, crosslines 196–996); Fold 40 → 20 offset classes, pre-stack and post-stack volumes | Marine acquisition standards; Amplitude preservation; AVO-optimized processing |
| 4.2 | Well data and logging | 8 wells (BS-01 to BS-16H), Sonic (DT), density (RHOB), gamma-ray logs; Gardner equation for missing density data | Strategic distribution; Environmental corrections; LAS/ASCII standardization |
| 4.3 | Petrophysical analysis | Mineral volumes: clay, calcite, dolomite, sandstone; Water saturation, effective porosity, lithofacies classification; multi-mineral interpretation algorithms | Core-calibrated validation; Formation-specific parameters; Consistent classification criteria |
| 4.4 | Seismic interpretation | Complete Ghar Formation time-domain mapping; Deterministic wavelet extraction, final TDRs; Structural framework and geological control | Geological consistency; Reflectivity-based calibration; Well-seismic tie optimization |
| 4.5 | Fluid contacts | Fluid contacts and + Velocity equation (Depth-to-time conversion) | MDT and DST resistivity logs (Fluid contacts) |

reveals consistent identification of an optimal chi angle of 32° across the majority of wells in the study area, demonstrating remarkable coherence in the EEI response to water saturation variations within the Ghar formation. The comprehensive analysis was performed across all eight wells in the study area, with six wells (BS-01, BS-02, BS-03, BS-06, BS-09, and BS-16H) demonstrating acceptable correlation trends between effective water saturation (SWE) and total water saturation (SWT) parameters (Fig. 3). However, certain wells, notably well BS-10 and BS-04, exhibit deviation from the general trend due to local geological complexities, particularly fault-related effects including mechanical fracturing that alters elastic properties, localized fluid redistribution along fault conduits, stress-induced velocity anisotropy, and sub-seismic heterogeneity that disrupt the systematic EEI-water saturation relationship. The correlation analysis results and systematic variation of correlation coefficients with chi angle are illustrated in Fig. 4, demonstrating the clear identification of optimal values for quantitative fluid discrimination in the Bahregansar Field.

## EEI analysis

Extended Elastic Impedance represents a significant advancement in quantitative seismic interpretation, building upon the foundation of conventional elastic impedance methodology. The elastic impedance technique computes acoustic impedance at variable incidence angles within the pre-stack domain through linear approximation of the Zoeppritz equations, providing a reliable framework for calibrating and inverting angle stacks (Connolly 1999). The fundamental approach involves computing an elastic impedance seismic attribute as an angle-dependent weighted product of velocity, S-velocity, and density, whereby the elastic inversion transforms pre-stack gathers into elastic impedance values for different incident angles (Whitcombe et al. 2002b). However, conventional elastic impedance methodology encounters limitations related to variable dimensionality that varies with incident angle, resulting in values that do not scale correctly across different angles (Whitcombe 2002a). The Extended Elastic Impedance approach addresses these fundamental limitations by eliminating dimensionality dependence through normalization with reference constants $V_{P0}$, $V_{S0}$, and $\rho_0$. The EEI function of normalized impedance values for all incident angles $\chi$ related to P-wave velocity $V_P$, S-wave velocity $V_S$, and density $\rho$ is expressed as:

$$\mathrm{EEI}\,(\chi) = \left(\frac{V_P}{V_{P0}}\right)^{(\cos^2\chi+\sin^2\chi\tan\chi)} \times \left(\frac{V_S}{V_{S0}}\right)^{-8\sin^2\chi} \times \left(\frac{\rho}{\rho_0}\right)^{\cos^2\chi-4\sin^2\chi} \tag{1}$$

The conventional elastic impedance approximation demonstrates effectiveness only for physical properties of rock within an incidence angle range of 0°–30° for pre-stack gathers, with no equivalent real value of angle beyond $\sin^2\theta$ limitations (Whitcombe et al. 2002b; Alebouyeh and Chehrazi 2018). To overcome this angular range limitation, Extended Elastic Impedance substitutes $\sin^2\theta$ with $\tan\chi$ in the two-term linearized Zoeppritz formulation:

$$\mathrm{R}\,(\chi) \approx \mathrm{A} \ + \mathrm{B}\tan\chi \tag{2}$$

This reformulation extends the definition from $\pm\infty$ rather than the 0–1 constraint imposed by $\sin^2\theta$. To ensure reflectivity values never exceed unity, a scaled version of reflectivity is defined as normal reflectivity multiplied by cos $\chi$. The EEI equation for scaled reflectivity RS at $\chi$ angles related to intercept A and gradient B becomes:

$$\mathrm{EEI}\,(\chi) \approx \mathrm{RS}\,(\chi) = (\mathrm{A}\cos\chi + \mathrm{B}\cos\chi\sin\chi) \tag{3}$$

The chi angle parameter varies between −90° and +90°, where EEI ($\chi$=0°) corresponds to acoustic impedance and EEI ($\chi$=90°) relates to gradient impedance. The Extended Elastic Impedance methodology enables application at different $\chi$ values to achieve approximate proportionality to various elastic parameters, including acoustic impedance, shear impedance, bulk modulus, shear modulus, Lamé parameters, and $V_P/V_S$ ratio. This technique facilitates maximum discrimination between lithology and fluid characteristics as EEI curves at different $\chi$ angles demonstrate proportionality to various rock elastic parameters. The optimal range of $\chi$ values can be determined through maximum cross-correlation analysis of EEI curves with petrophysical parameters such as shale volume, water saturation, and porosity, or with elastic parameters. Research indicates that bulk modulus and Lamé constant parameters typically occur within EEI space with $\chi$ values ranging from approximately 10° to 30°, while shear modulus and $V_P/V_S$ ratio parameters are found within $\chi$ ranges from approximately −30° to −90° and around 45°, respectively (Whitcombe et al. 2002b). These specific angular ranges represent optimal detection zones for fluid and lithology impedance functions. The implementation of Extended Elastic Impedance analysis requires a systematic determination of optimal $\chi$ angles through comprehensive cross-correlation analysis with target petrophysical parameters. The methodology involves generating EEI logs across the complete angular spectrum from −90° to +90° to evaluate cross-correlation relationships. Cross-correlation analysis of EEI logs with objective parameters enables identification of maximum correlation coefficients for target parameters, facilitating selection of optimal implementation angles for reservoir

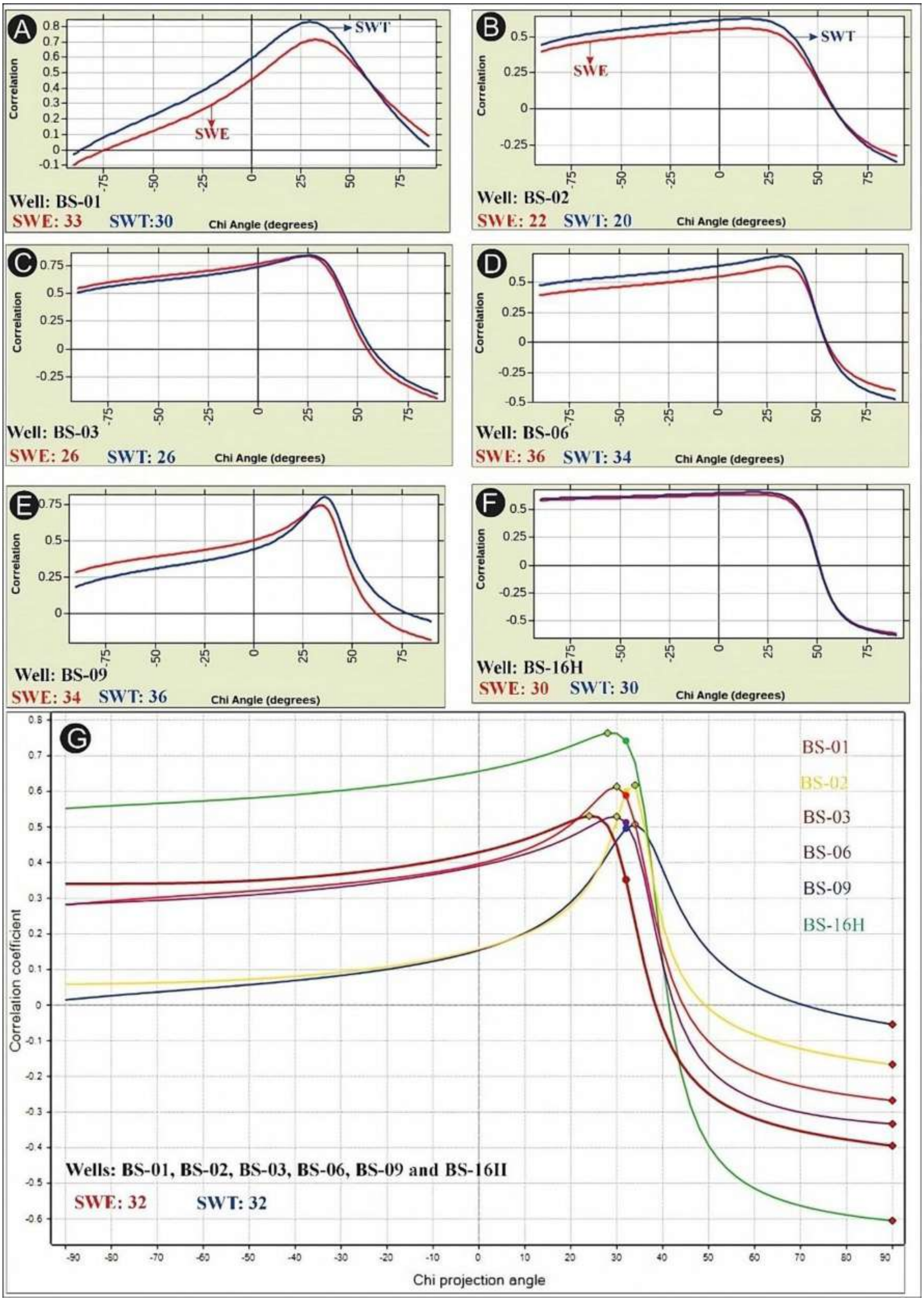


**Fig. 3** Six wells (BS-01, BS-02, BS-03, BS-06, BS-09, and BS-16H) demonstrate optimal chi angle calculation at 32° with aceptable correlation trends between SWE and SWT parameters, enabling reliable water saturation estimation through Extended Elastic Impedance analysis in the Ghar formation (Chi angle estimation plot: (**A**) BS-01, (**B**) BS-02, (**C**) BS-03, (**D**) BS-06, (**E**) BS-09, (**F**) BS-16H and (**G**) All acceptable wells plot)

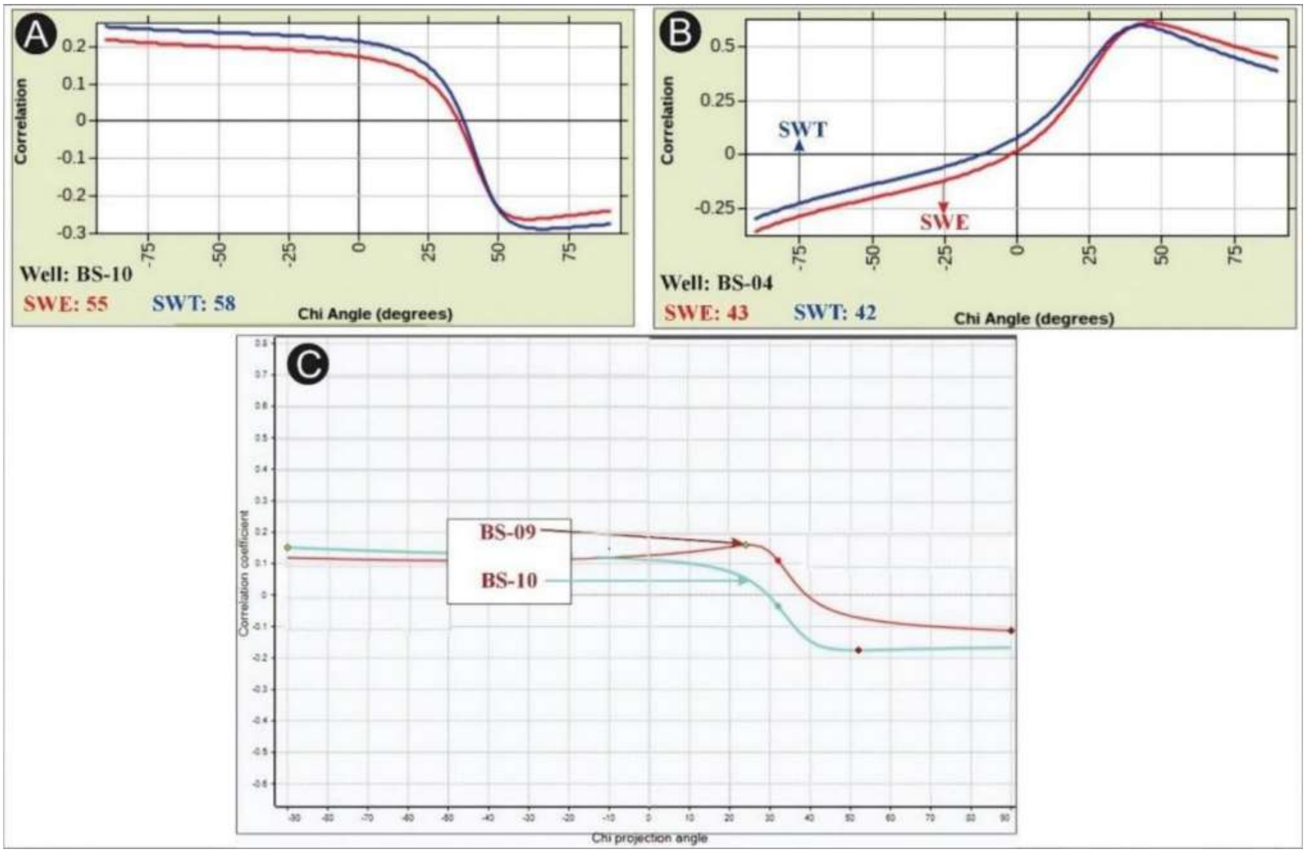


Fig. 4 Wells BS-10 and BS-04 show deviation from optimal chi angle trends due to local tectonic complexities and fault-related effects, resulting in altered elastic property relationships that compromise the standard EEI analysis approach for water saturation determination. **(A)** BS-10 and **(B)** BS-04, and **(C)** overall view of BS-10 and BS-04 Chi angle

characterization (Alebouyeh and Chehrazi 2018). Quality control procedures for selected χ angles incorporate EEI log spectrum analysis to create comprehensive reflectivity value spectra across all χ angle values, identifying the most reasonable angle values for specific applications. Additional quality control involves generating EEI logs for each target parameter at selected angles of maximum correlation, ensuring acceptable similarity with well log curves particularly within reservoir intervals, thereby validating the reliability of angle calculations (Figs. 5 and 6).

## AVO attribute development for enhanced fluid analysis

AVO (Amplitude Versus Offset) analysis examines reflected wave amplitude variations with source-receiver distance to detect petrophysical rock properties in reservoirs. The method relies on the Zoeppritz equations, which describe elastic wave behavior at subsurface interfaces through linearized approximations that yield intercept (A), gradient (B), and curvature (C) parameters from pre-stack seismic data. The systematic AVO classification framework provides a geological interpretation context through four distinct anomaly classes. Class I anomalies exhibit high acoustic impedance contrasts with positive intercept and negative gradient signatures, typically found in gas-saturated sandstone reservoirs overlain by low-impedance shales. Class II anomalies show negative intercept and positive gradient characteristics, representing challenging detection scenarios where gas sands occur within similar impedance shale sequences. Class III anomalies demonstrate negative intercept and gradient values when gas-saturated reservoirs underlie high-impedance formations. Class IV anomalies display positive intercept and gradient signatures, often associated with hydrocarbon micro-seepage effects or shallow gas accumulations. Advanced AVO attributes extend beyond basic intercept and gradient parameters to provide enhanced hydrocarbon detection and fluid discrimination capabilities. The Fluid Factor combines AVO intercept and gradient terms through a weighted formulation (A+kB), where coefficient k is optimized to maximize pore fluid sensitivity while reducing lithological effects. This attribute leverages differential elastic property responses to fluid substitution, enabling superior discrimination between hydrocarbon and water-saturated reservoirs. Gas Indicator attributes employ mathematical transformations of AVO

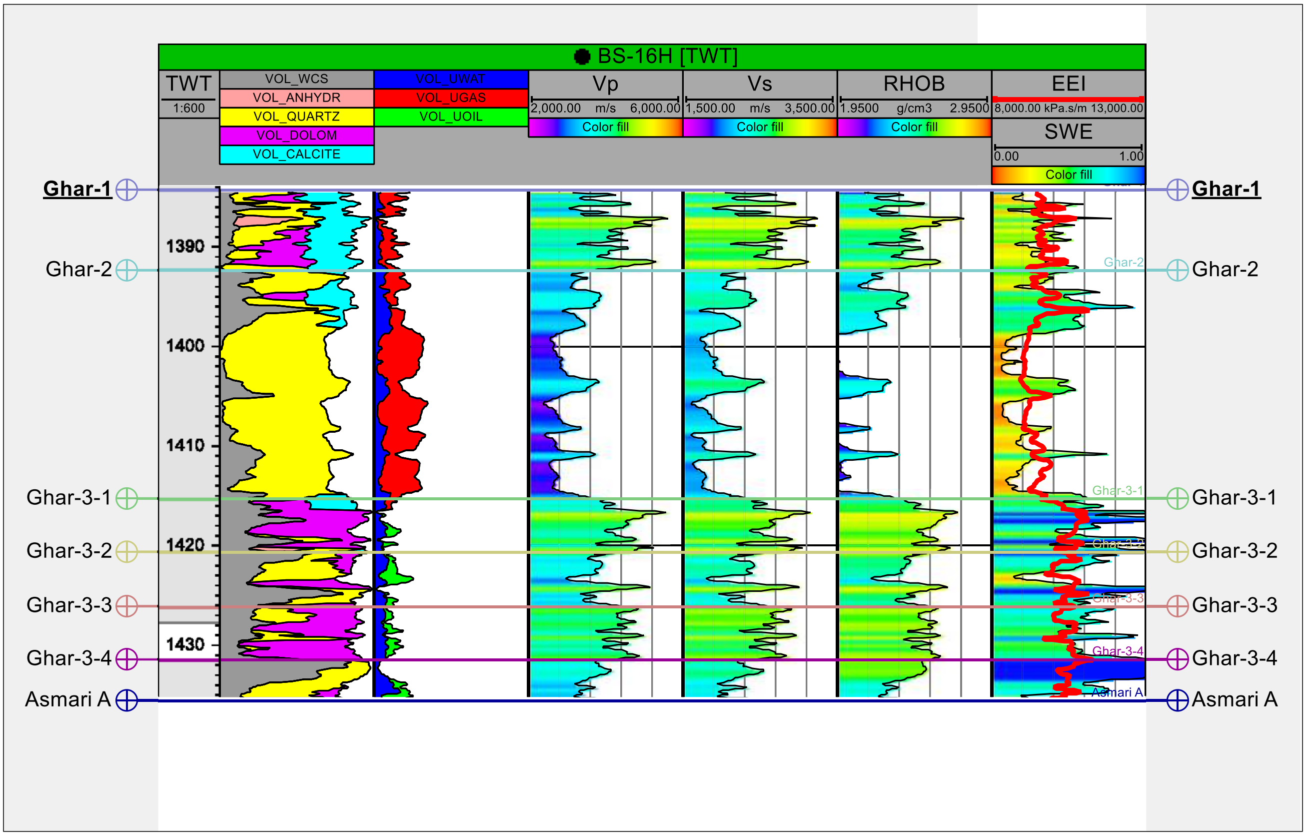


**Fig. 5** Correspondence between Extended Elastic Impedance (EEI) and water saturation (SWE) logs in well BS-16H, demonstrating validation of optimal chi angle (32°) with acceptable similarity between EEI and SWE trends within the Ghar formation reservoir interval

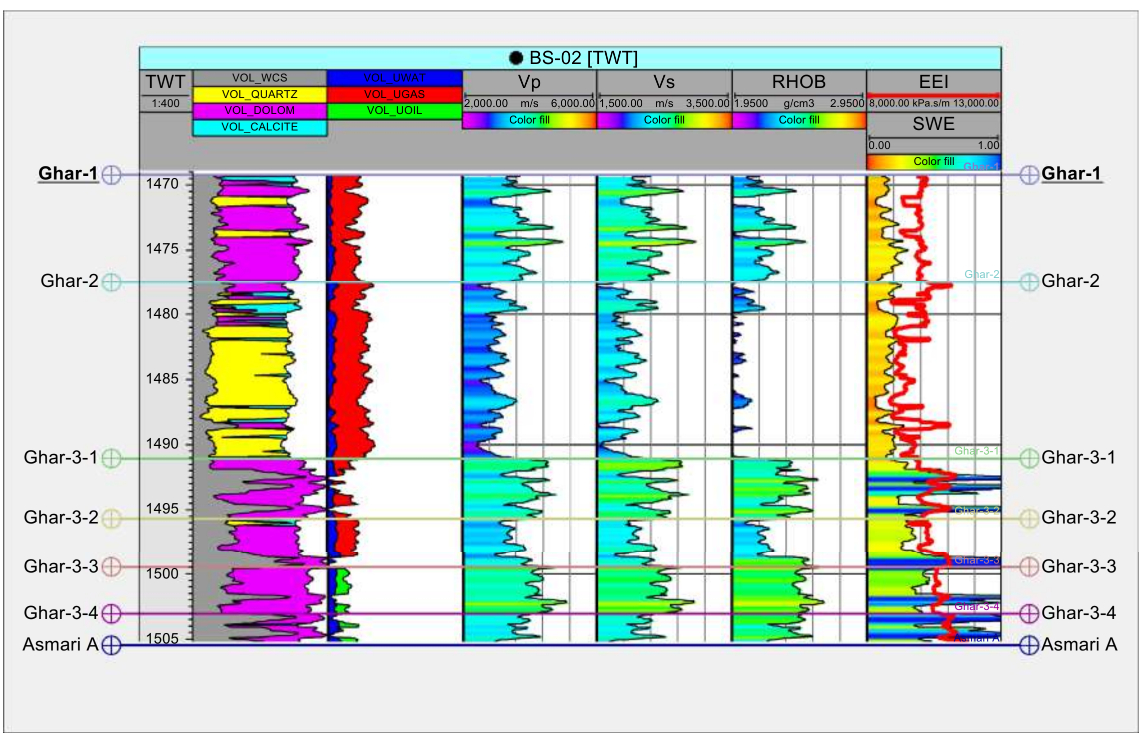


**Fig. 6** Correspondence between Extended Elastic Impedance (EEI) and water saturation (SWE) logs in well BS-02, showing validation of optimal chi angle (32°) through acceptable correlation between EEI and SWE trends within the reservoir interval

parameters specifically designed to enhance gas-related seismic signature detection. These attributes integrate local rock physics relationships and utilize threshold-based functions to highlight anomalous AVO behaviors characteristic of gas accumulations, requiring precise calibration with regional geological conditions. Poisson's Ratio Contrast (PRC) offers a physics-based fluid discrimination approach by exploiting gas saturation sensitivity in Poisson's ratio variations. Gas replacement of liquid phases dramatically reduces bulk modulus in pore spaces, creating detectable seismic signatures. PRC transforms intercept and gradient parameters into Poisson's ratio reflectivity using linearized relationships, providing direct rock physics interpretation for fluid characterization. Comparative analysis reveals distinct effectiveness in fluid discrimination capabilities across different AVO attributes (Rutherford and Williams 1989; Castagna and Swan 1997). The Intercept attribute provides acoustic impedance contrast information but shows limited sensitivity to fluid variations in tight reservoir conditions. The Gradient attribute demonstrates superior performance in detecting fluid-related Poisson's ratio changes, particularly effective in Class II and III AVO anomalies. The Fluid Factor exhibits enhanced discrimination power by amplifying hydrocarbon-related signatures while suppressing lithology effects (Smith and Gidlow 1987). Gas Indicator attributes show specific sensitivity to low-impedance gas accumulations through weighted AVO parameter combinations (Goodway et al. 1997). Poisson Ratio contrast demonstrates exceptional fluid discrimination capabilities by directly relating to pore fluid properties through $V_P/V_S$ ratio variations, proving most effective in clean sandstone reservoirs with significant porosity (Chopra and Castagna 2014). The implementation of these advanced AVO attributes in the Bahregansar Field analysis successfully demonstrates their effectiveness in identifying hydrocarbon-bearing zones within the Ghar sandstone reservoir system. The integrated interpretation provides robust fluid characterization, with each parameter contributing unique sensitivities to different geological scenarios. Secondary attributes such as fluid factor and scaled Poisson's ratio calculations enhance hydrocarbon detection sensitivity (Farfour and Foster 2022). Gas fluid discrimination boundaries are specifically delineated on geophysical maps (Figs. 7, 8, 9 and Figs. 11 and 12). The location map for all these figures is shown in Fig. 10.

Additionally, Figs. 11 and 12 show the maps and seismic sections of the Intercept and Gradient attributes at target horizon (Ghar-2), respectively. Gas fluid zones are clearly identified and outlined with yellow-colored boundaries, representing areas with high confidence for gas saturation based on comprehensive AVO attribute analysis. Oil fluid zones are delineated with white-colored boundaries, indicating regions with probable oil accumulation characteristics derived from the integrated interpretation of these two fundamental AVO attributes. The systematic color-coded framework demonstrates the effectiveness of Intercept and Gradient attributes in fluid discrimination, where these parameters provide complementary sensitivities to different hydrocarbon types within the Ghar sandstone reservoir system.

## EEI attributes generation using extracted (chi) angle

In quantitative seismic interpretation frameworks, seismic-derived attributes serve as fundamental tools for establishing correlative relationships between wellbore data and determining reservoir characteristics in areas with limited direct well control (Russell 1988). These attributes span diverse applications ranging from direct seismic inversion products, including acoustic velocity and bulk density, to specialized AVO parameters utilized in hydrocarbon detection studies (Chopra and Marfurt 2007). The current analysis employs the Extended Elastic Impedance (EEI) methodology, which enables the generation of reservoir and geological parameter volumes representing lithofacies and fluid property distributions through systematic application of optimized chi angles derived from petrophysical log analysis to AVO attribute datasets across the complete three-dimensional seismic volume (Whitcombe et al. 2002b). This approach facilitates spatial extrapolation of reservoir property relationships established at discrete well locations throughout the entire survey area, providing comprehensive subsurface characterization capabilities (Connolly 1999).

The analytical workflow involves rigorous application of the optimal chi angle parameter to the integrated seismic dataset, enabling extension of wellbore-calibrated reservoir models into inter-well regions through physics-based attribute transformations (Avseth et al. 2010). The methodology acknowledges that analytical outputs represent relative trends and parameter variations rather than absolute quantitative measurements, which nevertheless provide substantial interpretive significance for reservoir delineation and fluid discrimination applications (Avseth et al. 2010). The resulting spatial distribution patterns and geological trends are comprehensively illustrated through maps and seismic sections presented in Fig. 13.

## Unsupervised PNN analysis for fluid distribution mapping

As the conclusive phase of the quantitative fluid discrimination workflow, Probabilistic Neural Network (PNN) analysis was implemented through a semi-supervised learning approach to generate comprehensive oil, gas, and water

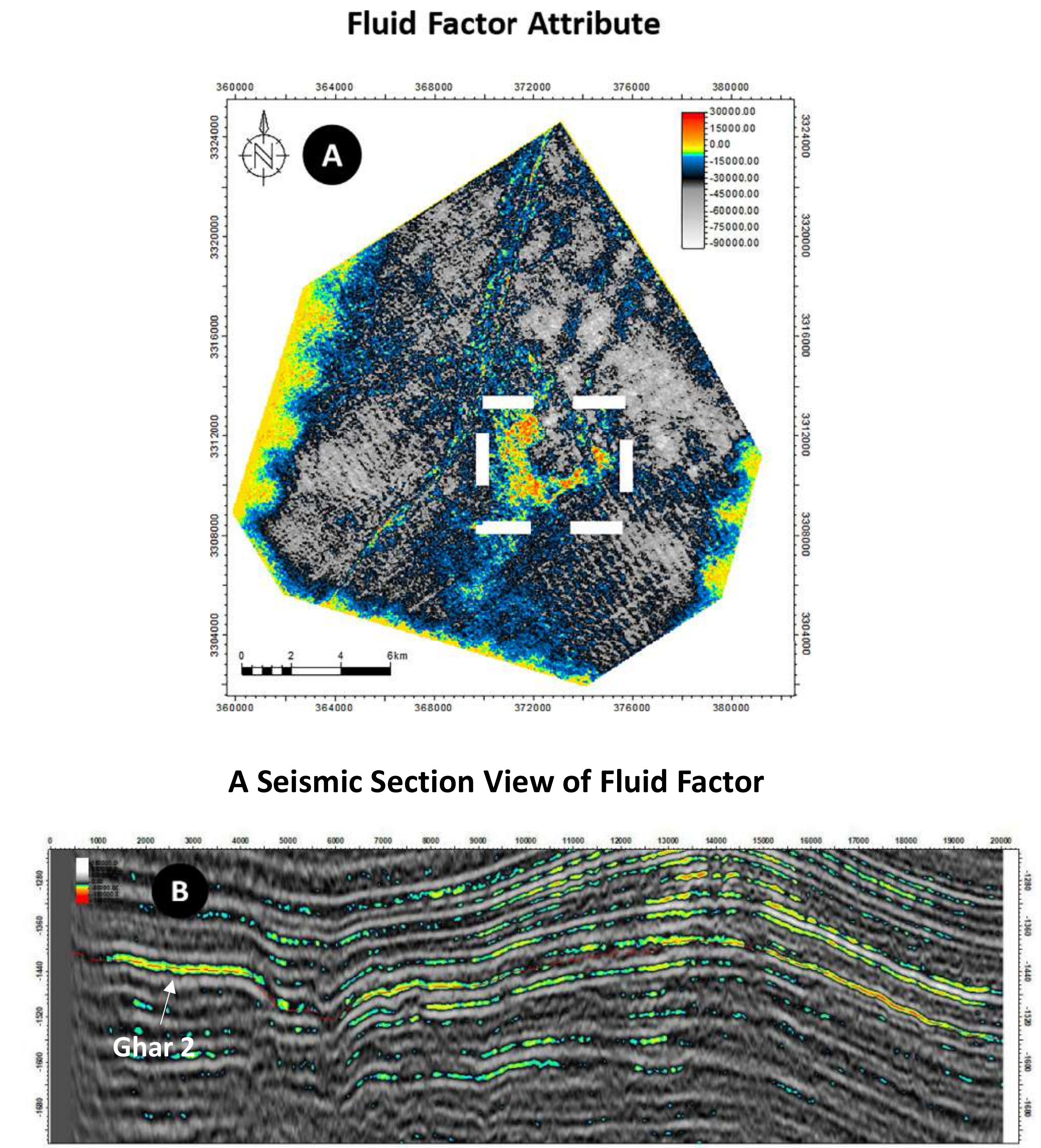


**Fig. 7** Fluid Factor AVO attribute at target horizon (Ghar-2): (**A**) attribute map showing gas fluid discrimination boundaries delineated in the structural crest and southern flank, and (**B**) seismic section view displaying Fluid Factor response along the Ghar-2 horizon with location shown in Fig. 10

distribution maps with associated probability estimates (Specht 1990; Hampson et al. 2001).

PNN Architecture and Rationale: The PNN implements a four-layer architecture based on Bayesian decision theory: (1) an input layer with six normalized seismic attributes (EEI at $\chi = 32°$, intercept, gradient, fluid factor, gas indicator, Poisson's ratio contrast), (2) a pattern layer storing all training samples as Gaussian kernel neurons ($\varphi(x) = \exp(-\|x - xi\|^2/2\sigma^2)$) that compute similarity between input and stored patterns, (3) a summation layer with three neurons

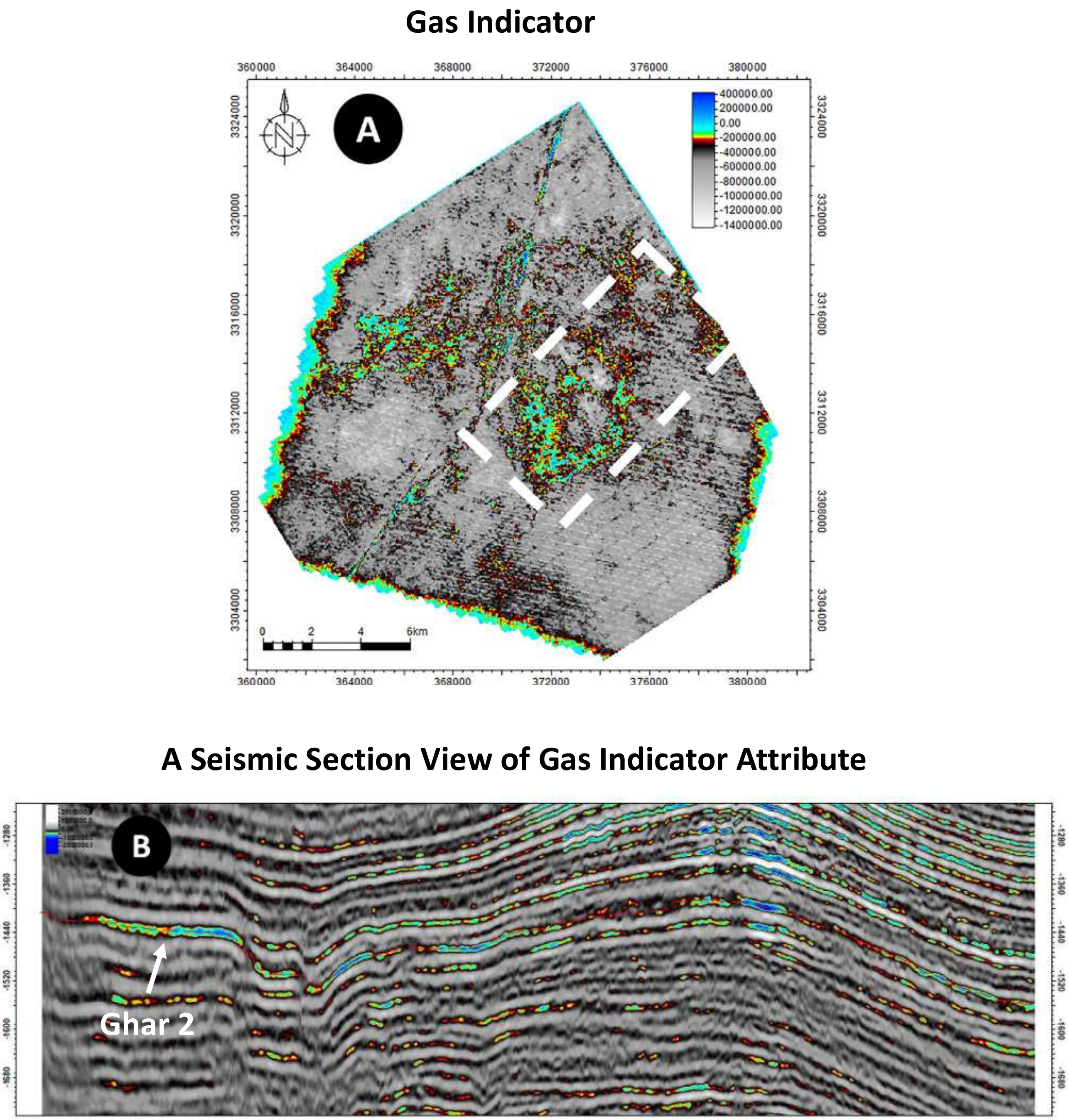


**Fig. 8** Gas Indicator AVO attribute at target horizon (Ghar-2): (**A**) attribute map highlighting gas-related Poisson's ratio variations concentrated in structural crest and western flank areas, and (**B**) seismic section view showing Gas Indicator response along the Ghar-2 horizon with location shown in Fig. 10

(oil, gas, water) aggregating pattern outputs to estimate probability densities, and (4) an output layer providing probabilistic classifications P(Oil), P(Gas), P(Water) summing to unity. The PNN was selected over alternative approaches for its inherent probabilistic output enabling uncertainty quantification, effective performance with sparse training data (six wells), non-iterative training eliminating convergence issues, robustness to noisy seismic data through Gaussian kernel smoothing, computational efficiency for large 3D volumes, and transparent decision-making based on pattern similarity facilitating geological validation (Specht 1990).

Training Data Preparation: Training data were derived from six well locations (BS-01, BS-02, BS-03, BS-06, BS-09, BS-16H) demonstrating reliable elastic

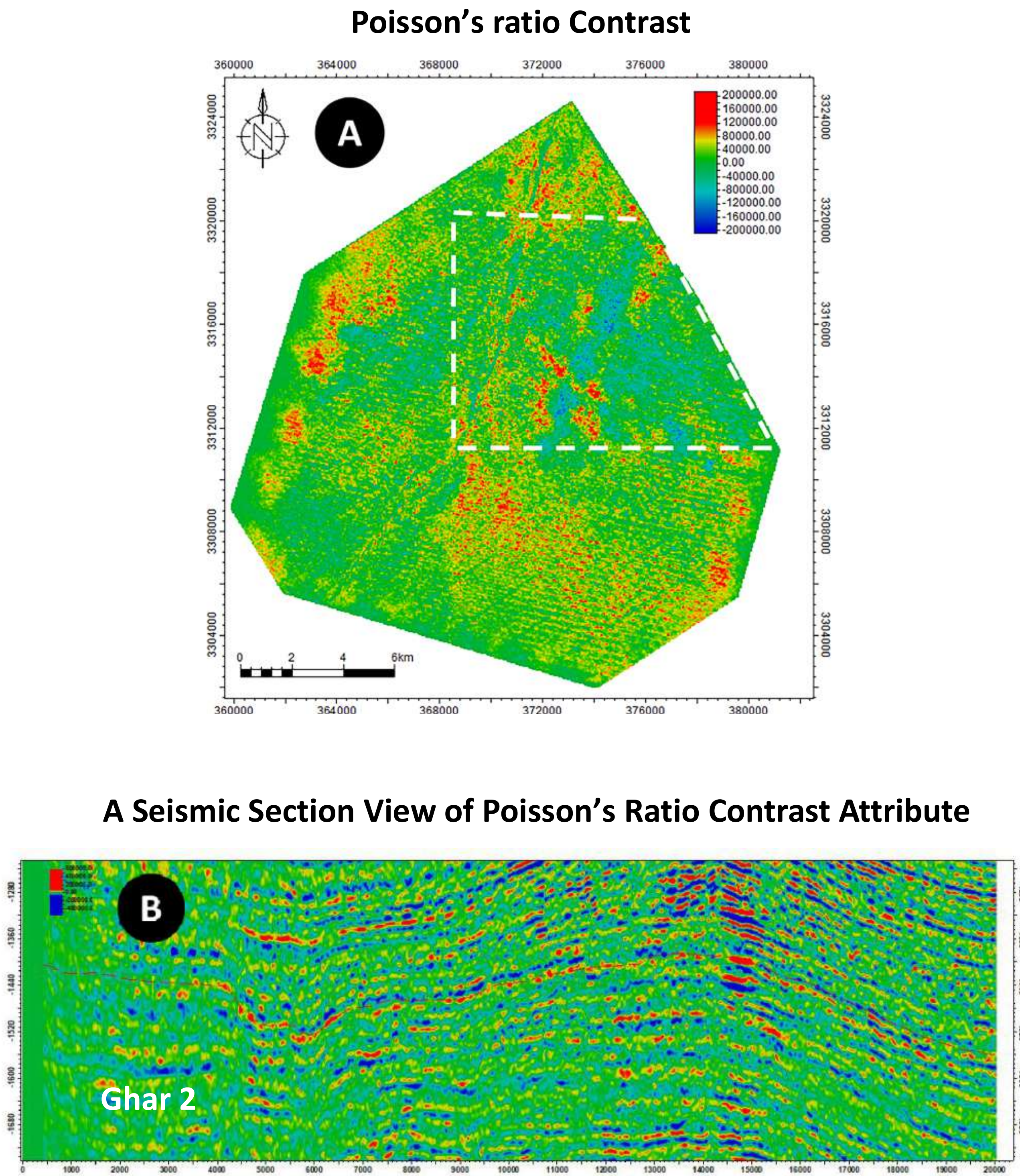


**Fig. 9** Poisson's Ratio Contrast (PRC) attribute at target horizon (Ghar-2): (**A**) attribute map showing Poisson's ratio variations associated with fluid and lithological effects, and (**B**) seismic section view displaying PRC response along the Ghar-2 horizon with location shown in Fig. 10

property-fluid saturation correlations (Sect. "Optimal Chi Angle Determination for Extended Elastic Impedance Analysis"). Wells BS-04 and BS-10 were excluded due to fault-related effects. Three fluid classes were defined: Gas (above GOC at − 2073 m TVDSS, SWE < 0.30), Oil (between GOC and OWC at − 2097 m TVDSS, 0.30 < SWE < 0.60), and Water (below OWC, SWE > 0.60). Training samples were extracted at regular depth intervals across the Ghar reservoir section, with each sample consisting of the 6-dimensional attribute vector paired with its fluid class label, maintaining

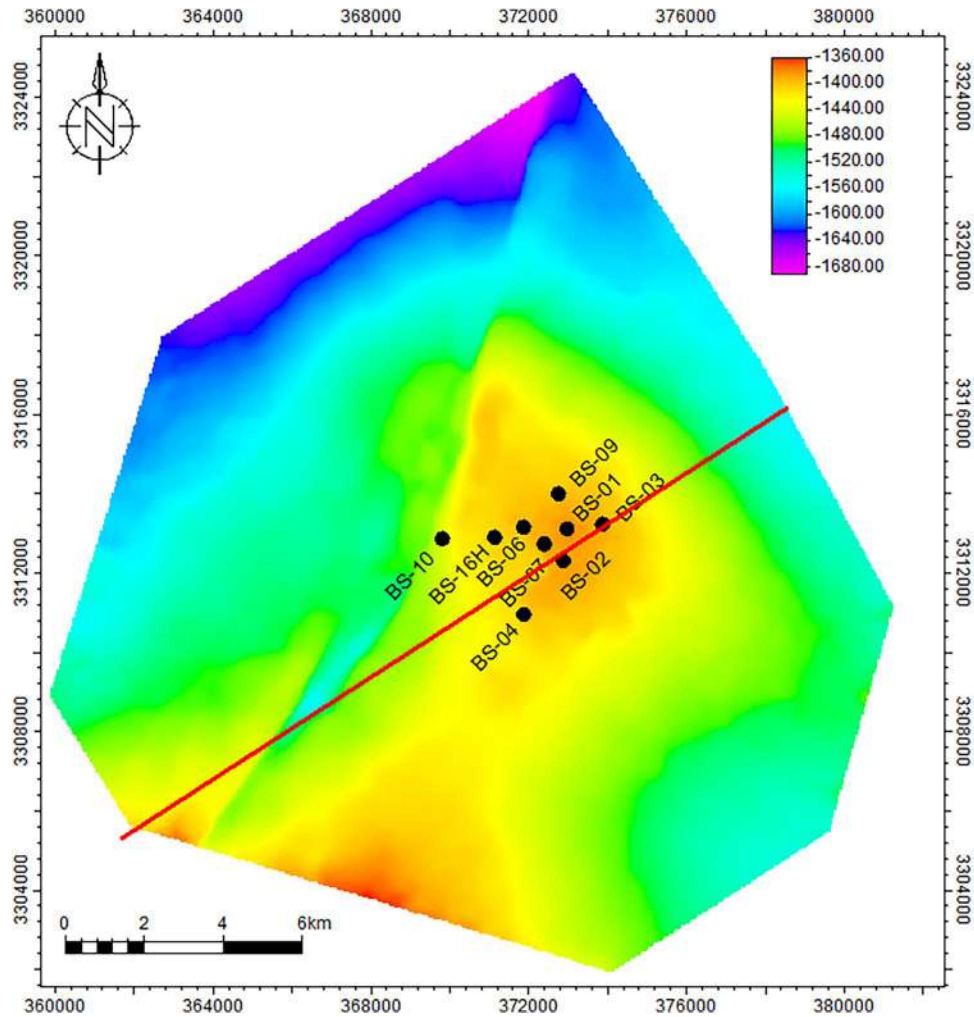


**Fig. 10** Location map of the Bahregansar field showing well positions (BS-01, BS-02, BS-03, BS-04, BS-06, BS-07, BS-09, BS-10, BS-16H) ad the position of the arbitrary seismic line used in Figs. 7, 8, 9, 11, 12, and 13

approximately balanced class distribution to prevent classification bias.

Supervised Training Phase: The initial supervised training established the baseline PNN model using exclusively labeled well data. The smoothing parameter (σ) controlling generalization characteristics was optimized through leave-one-well-out cross-validation: iteratively training on five wells while testing on the sixth excluded well, repeating for all six combinations, and selecting the σ value yielding maximum average accuracy across all folds. This ensures effective generalization to unseen well locations rather than memorizing specific training well characteristics.

Semi-Supervised Learning Methodology: The semi-supervised framework addresses the fundamental seismic interpretation challenge of extensive seismic coverage (hundreds of thousands of traces) with limited well control (six labeled wells). The iterative process begins by applying the supervised PNN to the entire 3D seismic volume, generating probability estimates at every trace. High-confidence predictions (where maximum probability significantly exceeds competing classes with geologically plausible spatial distribution and consistency with surrounding predictions) are identified and assigned as "pseudo-labels"—unlabeled samples predicted with sufficient confidence to treat as additional training data. The PNN is then retrained incorporating both original labeled well samples and high-confidence pseudo-labeled seismic samples, expanding the training dataset with both human-labeled and machine-labeled samples. This updated model is reapplied to the volume, generating revised probabilities that incorporate pseudo-labeled information. Iteration continues until convergence, defined when the percentage of traces changing classification falls below 5%, indicating model stability. Figure 18 A presents the training error and relative error evolution across 50 iterations, demonstrating systematic convergence with training error decreasing from 0.035 to approximately 0.027 and relative error stabilizing at 0.77 (Fig. 18B, C), confirming successful pseudo-label integration and validating semi-supervised learning stability.

Advantages and Outputs: The semi-supervised approach leverages abundant unlabeled seismic data to learn attribute-fluid relationships representative of the entire reservoir,

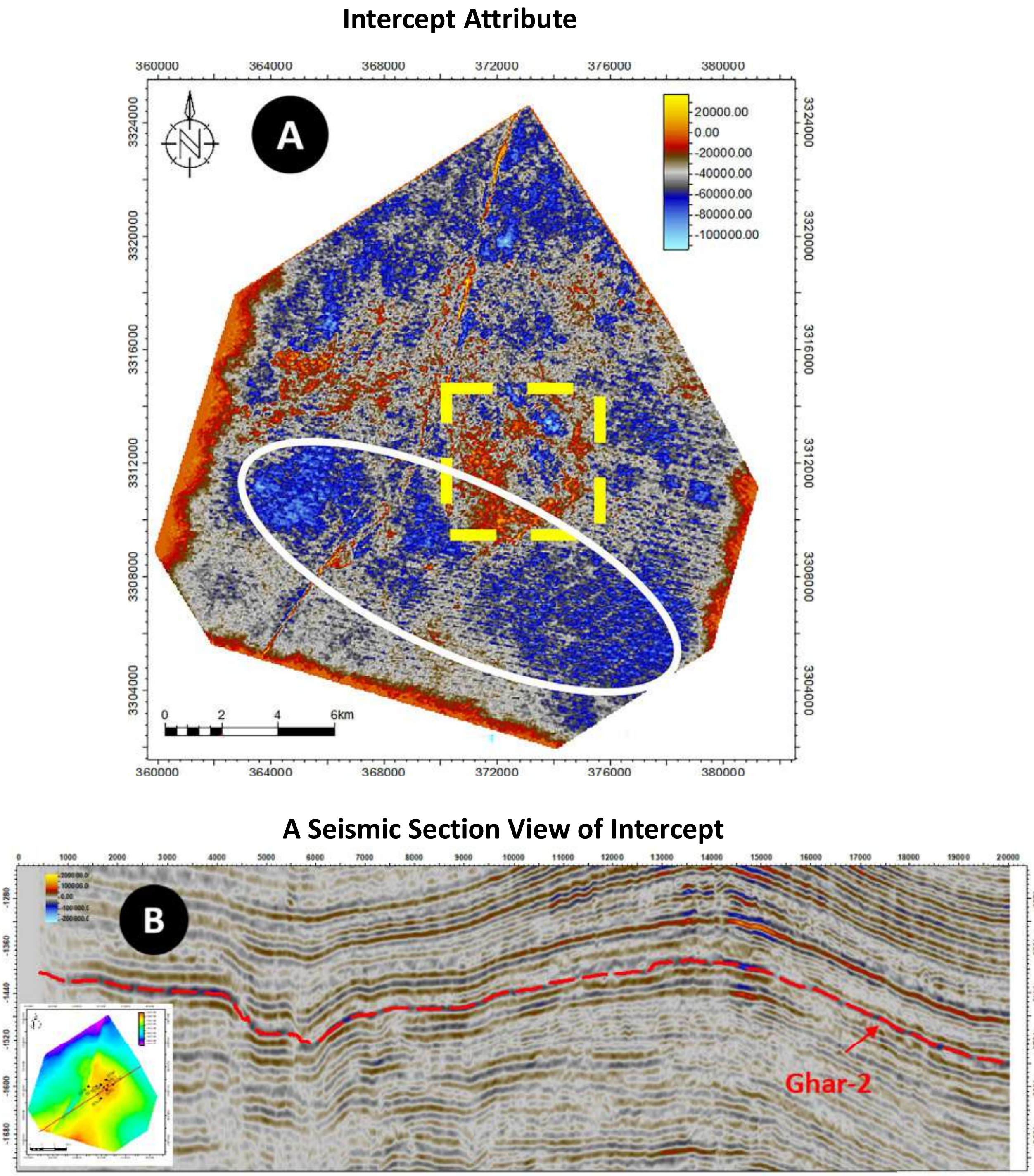


**Fig. 11** Intercept AVO attribute at target horizon (Ghar-2): (**A**) attribute map showing acoustic impedance contrast with fluid discrimination boundaries (yellow outline: gas zones; white outline: oil zones), and (**B**) seismic section view displaying Intercept response along the Ghar-2 horizon with location shown in Fig. 10

reducing overfitting to sparse well locations and enhancing prediction accuracy in areas distant from well control. The iterative pseudo-labeling naturally enforces spatial consistency aligning with geological expectations of continuous fluid contacts and stratigraphic control. The final model produces: (1) fluid classification volumes identifying most-likely fluid class at each location, (2) three probability volumes (P(Oil), P(Gas), P(Water)) enabling uncertainty quantification, (3) uncertainty maps highlighting ambiguous regions indicating geological complexity or areas requiring

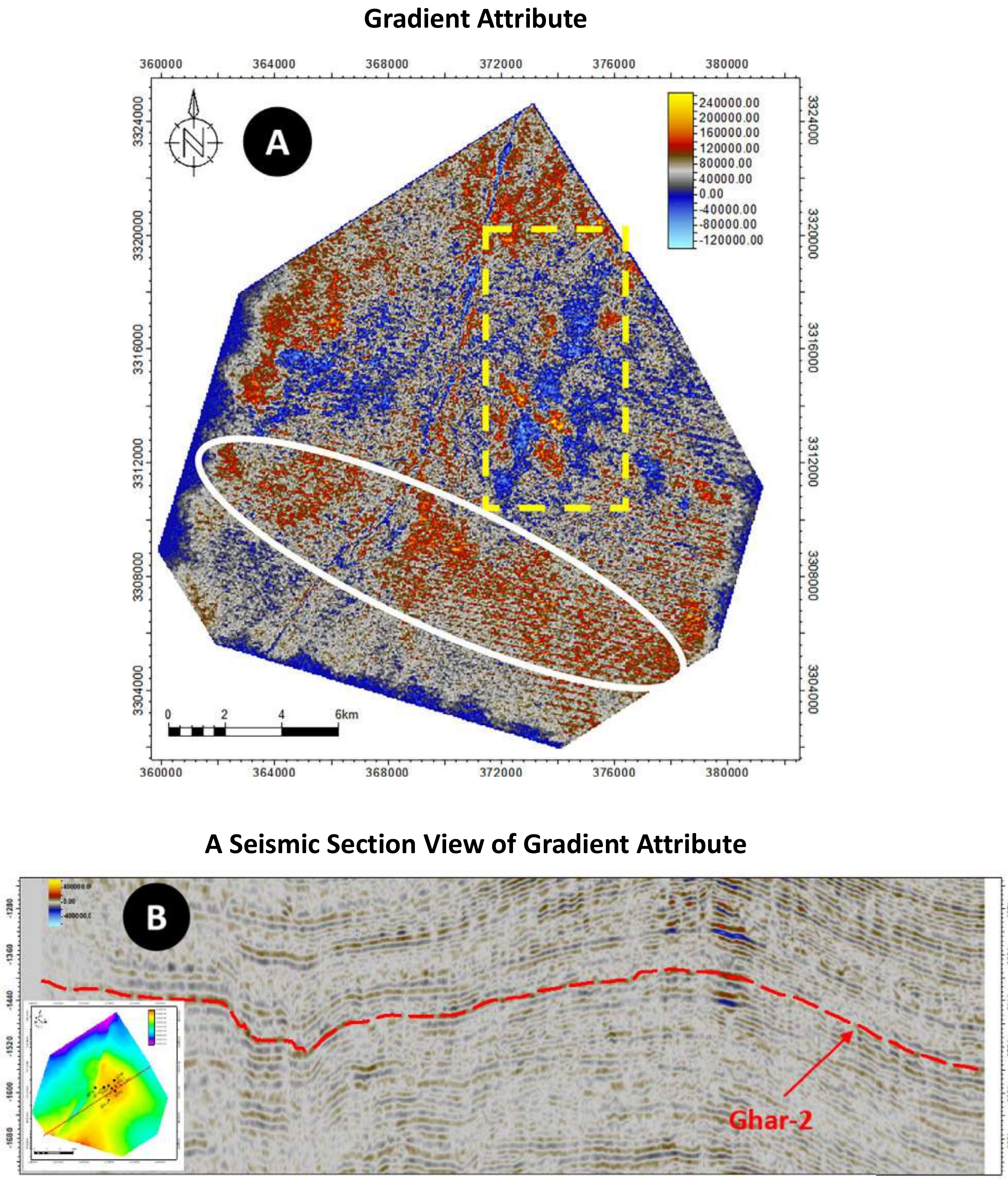


**Fig. 12** Gradient AVO attribute at target horizon (Ghar-2): (**A**) attribute map showing Poisson's ratio variations with fluid discrimination boundaries (yellow outline: gas zones; white outline: oil zones), and (**B**) seismic section view displaying Gradient response along the Ghar-2 horizon with location shown in Fig. 10

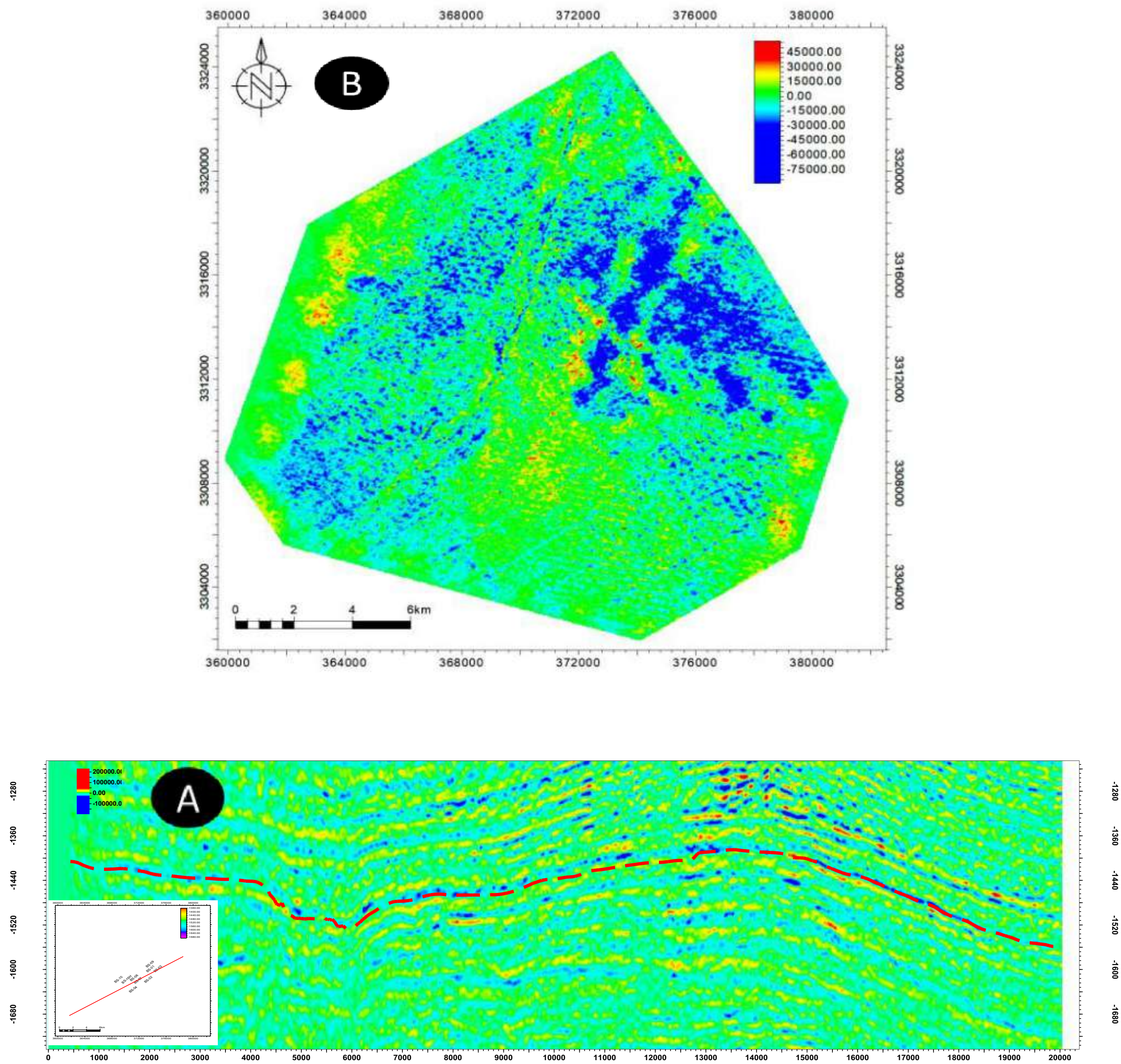


**Fig. 13** Extended Elastic Impedance (EEI) attribute using optimal chi angle (32°) at target horizon (Ghar-2): **A** attribute map showing spatial distribution with gas-bearing fluid zones clearly delineated, and **B** seismic section view of EEI attributes along the arbitrary line (location shown in Fig. 10), demonstrating clear identification of gas fluid zones

additional validation, and (4) confidence surfaces showing classification certainty.

Validation: Validation employed three complementary approaches: (1) Well-based validation through leave-one-well-out cross-validation ensuring generalization to unseen well locations, (2) Geological validation evaluating consistency with structural configuration (gas at crests, oil on flanks, water at base), fluid contact depths from pressure testing, production data, and stratigraphic architecture, and (3) Fluid contact validation—the most rigorous approach comparing predictions against independently determined contacts. Figure 11 illustrates excellent correspondence between gas-oil contact (GOC at − 2073 m TVDSS) and the boundary between gas (red) and oil (green) predictions, and oil–water contact (OWC at − 2097 m TVDSS) and the boundary between oil (green) and water (blue) predictions. This independent validation confirms the PNN's capability to accurately discriminate fluid types based on seismic

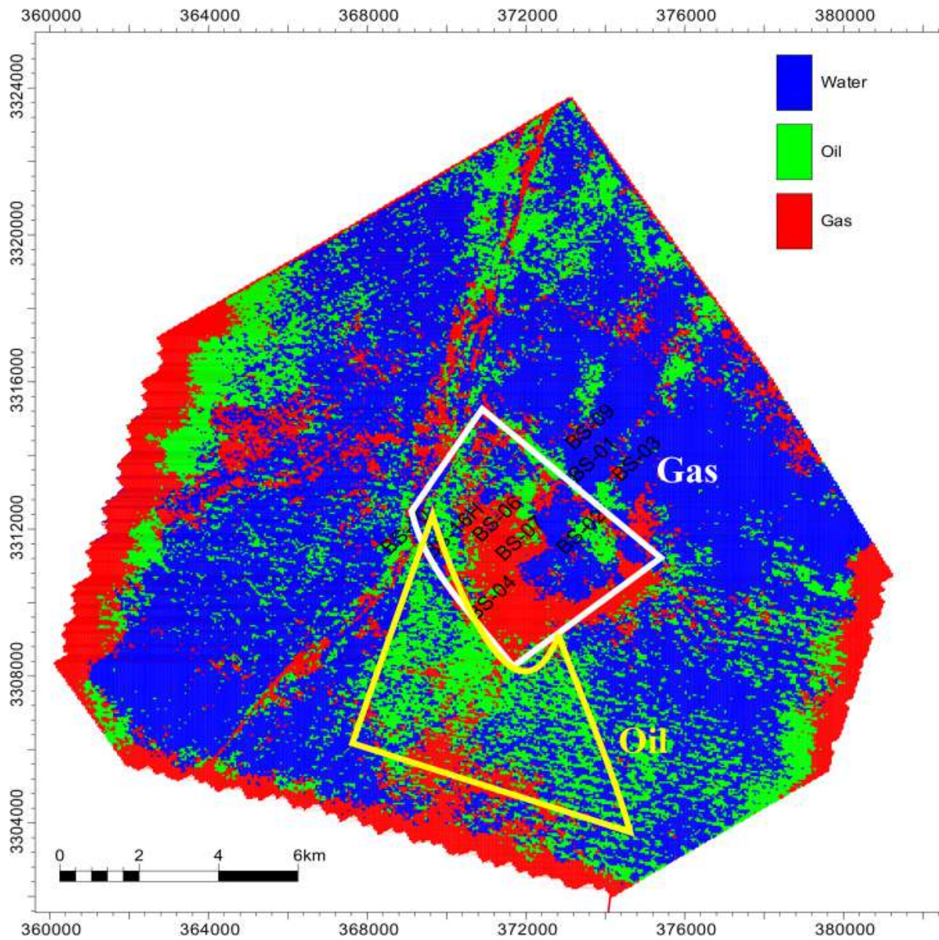


**Fig. 14** Three-dimensional integrated fluid facies map from Probabilistic Neural Network (PNN) analysis combining AVO and EEI attributes, showing comprehensive fluid distribution: gas (red zones concentrated in structural crest), oil (green zones along southern flank), and water (blue zones throughout broader reservoir interval) in the Ghar-2 sandstone reservoir

attributes, providing confidence in predictions throughout areas lacking direct well control.

Limitations: Four constraints affect result interpretation: (1) training wells concentrated in the structural crest potentially bias toward crest-area characteristics, with flank predictions carrying higher uncertainty; (2) the six-attribute input set balances discriminatory power with computational efficiency, though additional attributes might enhance discrimination; (3) the semi-supervised approach assumes high-confidence predictions are accurate, though convergence monitoring and fluid contact validation mitigate error propagation risks; and (4) PNN operates at seismic resolution (vertical: ~ 15 to 30 m, lateral: ~ 30 to 50 m) coarser than well log resolution (cm-scale), preventing detection of thin beds and small-scale heterogeneities below seismic resolution. Despite these limitations, the integrated approach successfully demonstrates quantitative fluid discrimination capabilities, providing a robust framework for reducing exploration risks and optimizing field development strategies in complex reservoir environments (Masters 1995; Russell et al. 2003; Chopra and Marfurt 2007).

## Results

This comprehensive study successfully integrated Extended Elastic Impedance (EEI) analysis with systematic seismic data interpretation and incidence angle analysis derived from well locations to establish a robust framework for reservoir fluid characterization. The methodology systematically computed and mapped AVO indicators across the reservoir, utilizing Poisson's ratio variations as a fundamental diagnostic tool for fluid presence assessment. Building upon these seismic-based insights, a semi-supervised

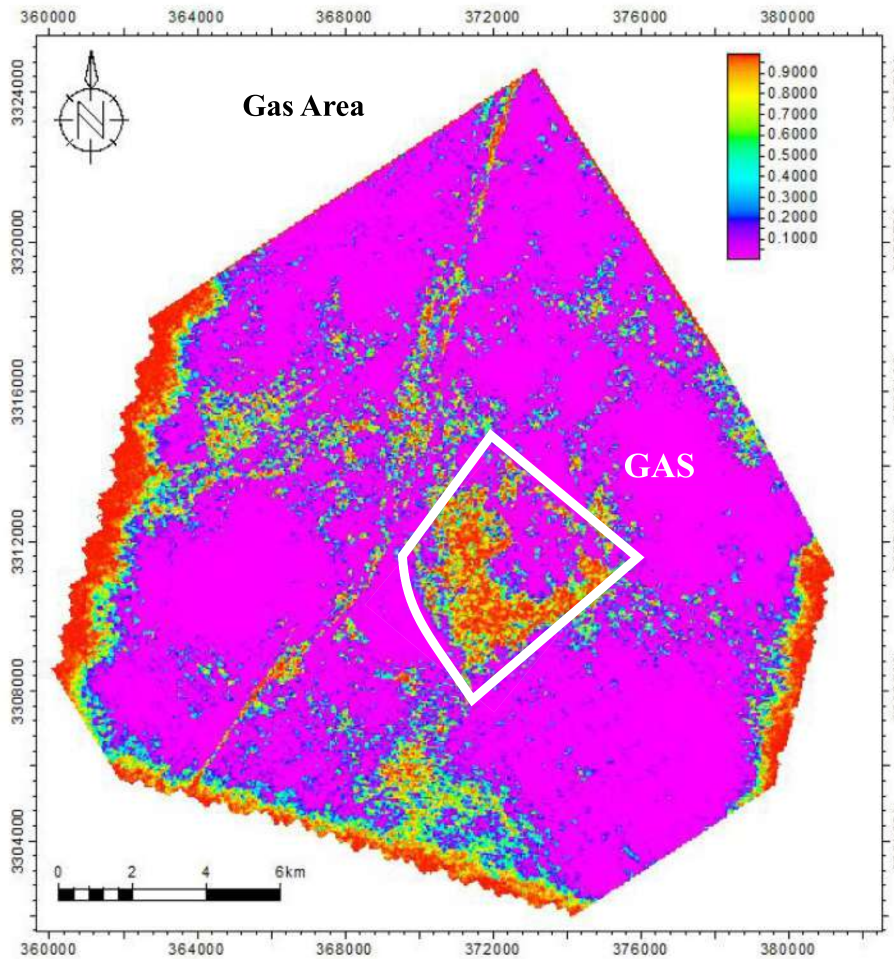


**Fig. 15** Gas fluid probability distribution map from semi-supervised PNN analysis at target horizon (Ghar-2), showing high-probability gas accumulation zones (delineated area) concentrated in the structural crest, with probability values ranging from 0.1 to 0.9. Well locations shown for reference (BS-01 through BS-16H)

Probabilistic Neural Network (PNN) framework was implemented to integrate all available datasets, generating comprehensive fluid distribution maps with associated probability distributions that effectively identify hydrocarbon accumulations and characterize water saturation variations throughout the reservoir.

The principal results demonstrate the effectiveness of this integrated approach through three key achievements. First, the comprehensive calculation of AVO and EEI indicators from seismic datasets generated detailed reservoir maps that, through integrated interpretation, enabled systematic evaluation of hydrocarbon presence probabilities across the entire field. Second, spatial fluid distribution was successfully characterized through the semi-supervised neural network integration, where well data provided essential constraints for incidence angle determination and EEI map construction while maintaining independence from the clustering algorithm, ensuring unbiased results. Third, the methodology revealed distinct and geologically meaningful fluid signatures, with gas accumulations (red zones) systematically concentrated in the structural crest, oil presence (green zones) delineated along the southern flank, and water distribution (blue zones) mapped throughout the broader reservoir interval. These findings collectively establish a validated workflow for reservoir fluid characterization that combines the strengths of seismic attribute analysis, machine learning integration, and geological understanding, providing a reliable foundation for field development and production optimization strategies.

The resulting 3D fluid distribution maps and probability volumes are illustrated in Figs. 14, 15, 16, 17, while the quantitative assessment of prediction accuracy and

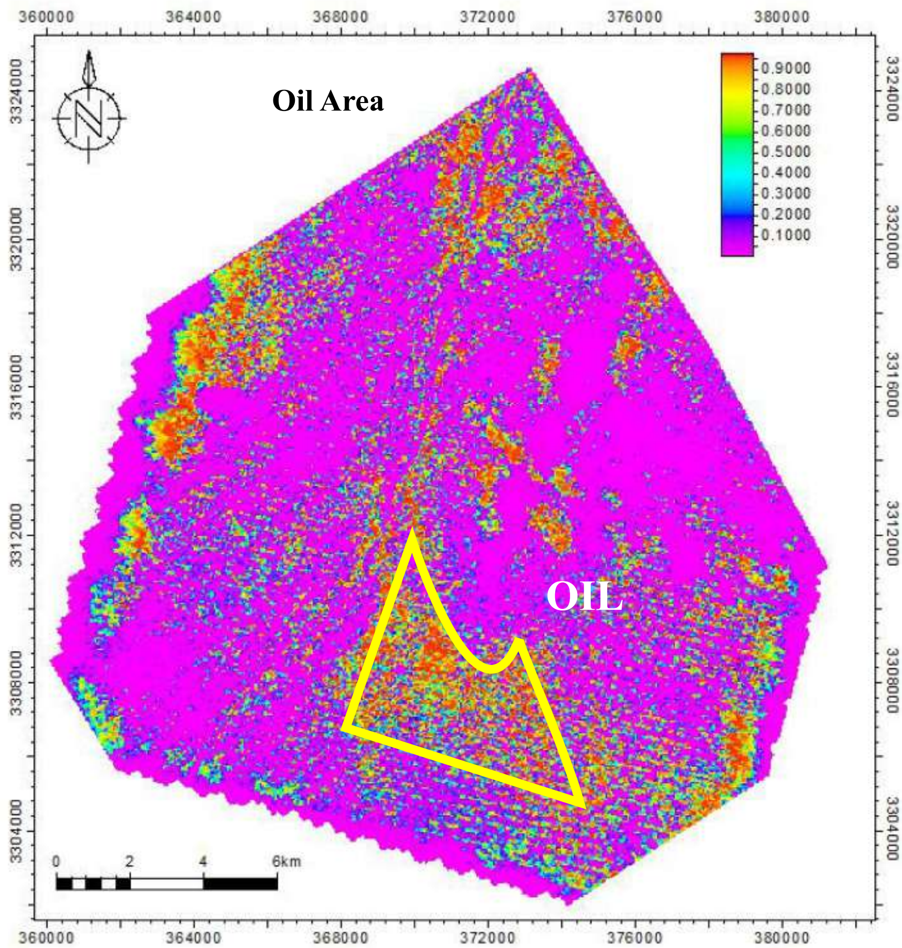


**Fig. 16** Oil fluid probability distribution map from semi-supervised PNN analysis at target horizon (Ghar-2), showing probable oil accumulation zones (yellow outlined area) along the southern structural flank, with probability values ranging from 0.1 to 0.9. Note: Uncertainty exists due to limited well control in this area

associated error statistics are summarized in Fig. 18, demonstrating the effectiveness of the integrated AVO/EEI and PNN approach for comprehensive fluid discrimination in the Bahregansar Field Ghar sandstone reservoir.

## Discussion

The fluid factor indicator demonstrates robust sensitivity to hydrocarbon presence within reservoir boundaries, exhibiting pronounced anomalies throughout both structural crest and southern flank regions (Fig. 7). The gas indicator reveals significant Poisson's ratio variations, suggesting substantial lithological or fluid property modifications, with gas-related signatures concentrated primarily in structural crest and western flank areas (Fig. 8). This enhanced sensitivity derives from the fundamental relationship between fluid saturation and Poisson's ratio, where gas substitution dramatically reduces bulk modulus values, creating detectable seismic signatures.

Comparative evaluation demonstrates distinct anomaly distribution patterns across the Bahregansar reservoir. Western flank regions show pronounced Poisson's ratio variations in gas indicator responses without corresponding fluid factor anomalies, indicating lithological rather than fluid-controlled effects (Fig. 9). Coincident anomalies in both indicators provide enhanced confidence for fluid presence interpretation, particularly for gas accumulation identification, as these dual responses typically characterize hydrocarbon-bearing reservoirs within the field. Southern flank

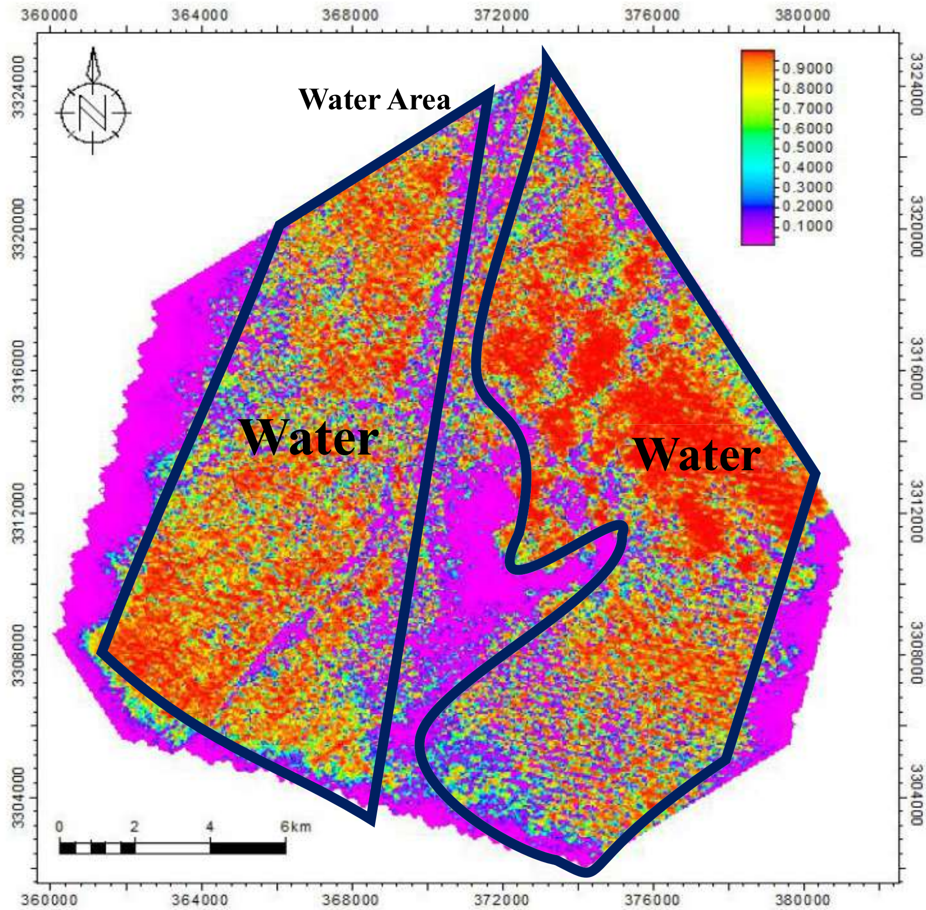


**Fig. 17** Water fluid probability distribution map from semi-supervised PNN analysis at target horizon (Ghar-2), showing water saturation zones (dark blue outlined areas) distributed throughout the broader reservoir interval, with probability values ranging from 0.1 to 0.9. Note: Uncertainty exists for water discrimination due to absence of well data and production information in these areas

fluid factor anomalies occur independently of gas indicator responses, suggesting fluid effects potentially associated with varying reservoir conditions, including pressure, temperature, and compositional variations specific to the Bahregansar formation characteristics.

These interpretations receive strong support from Poisson's Ratio Change (PRC) and Extended Elastic Impedance (EEI) analysis conducted across the field (Fig. 13). The PRC indicator mirrors gas indicator behavior through Poisson's ratio variations, while EEI effectively delineates water saturation trends through optimized chi-angle projections tailored to the reservoir properties. Cross-validation confirms that the southern flank Poisson's ratio and EEI variations correlate with fluid factor anomalies, exhibiting characteristics similar to crest area responses observed in the Bahregansar field. This correlation strongly supports fluid property variation as the controlling mechanism rather than lithological heterogeneity throughout the reservoir interval.

The PNN methodology with semi-supervised learning facilitated systematic interpretation of AVO and EEI distributions across the Bahregansar field. The integration of EEI and AVO attributes into the PNN framework was accomplished by combining the optimized EEI volume ($\chi = 32°$) with five AVO-derived attributes (intercept, gradient, fluid factor, gas indicator, Poisson's ratio contrast) to form a 6-dimensional feature space for each seismic trace, with all attributes normalized and fed as input vectors to the PNN for probabilistic classification, as detailed in Sect. "Unsupervised PNN Analysis for Fluid Distribution Mapping". Neural network analysis demonstrates that Poisson's ratio anomalies in the structural crest correspond to gas presence (red classification) (Figs. 14 and 15), while fluid factor and EEI variations along the southern flank indicate oil accumulation (green classification) (Figs. 14 and 16). Water presence (blue classification) characterizes the remaining reservoir areas, providing a comprehensive fluid distribution

A

| Iteration | Training Error | Relative Error | Iteration | Training Error | Relative Error |
|---|---|---|---|---|---|
| 1 | 0.03538 | 1 | 26 | 0.03061 | 0.86523 |
| 2 | 0.03501 | 0.98965 | 27 | 0.03044 | 0.86047 |
| 3 | 0.03488 | 0.98584 | 28 | 0.03027 | 0.8556 |
| 4 | 0.03456 | 0.97691 | 29 | 0.03015 | 0.85224 |
| 5 | 0.03439 | 0.97203 | 30 | 0.02998 | 0.84739 |
| 6 | 0.03414 | 0.96491 | 31 | 0.02984 | 0.84343 |
| 7 | 0.03386 | 0.95701 | 32 | 0.0297 | 0.83939 |
| 8 | 0.03372 | 0.95315 | 33 | 0.02956 | 0.83554 |
| 9 | 0.03347 | 0.9461 | 34 | 0.02941 | 0.83136 |
| 10 | 0.03336 | 0.94285 | 35 | 0.02927 | 0.82735 |
| 11 | 0.03309 | 0.93522 | 36 | 0.02914 | 0.82368 |
| 12 | 0.03293 | 0.93076 | 37 | 0.02904 | 0.8208 |
| 13 | 0.03267 | 0.92339 | 38 | 0.02885 | 0.81538 |
| 14 | 0.03257 | 0.92047 | 39 | 0.02868 | 0.81067 |
| 15 | 0.03235 | 0.91429 | 40 | 0.02857 | 0.80767 |
| 16 | 0.03217 | 0.90927 | 41 | 0.02843 | 0.80368 |
| 17 | 0.03198 | 0.90385 | 42 | 0.02831 | 0.80029 |
| 18 | 0.03189 | 0.90139 | 43 | 0.02814 | 0.79525 |
| 19 | 0.03172 | 0.89663 | 44 | 0.02802 | 0.79196 |
| 20 | 0.03154 | 0.89142 | 45 | 0.02788 | 0.78801 |
| 21 | 0.03131 | 0.88495 | 46 | 0.02773 | 0.78379 |
| 22 | 0.0312 | 0.88195 | 47 | 0.02744 | 0.7756 |
| 23 | 0.031 | 0.87632 | 48 | 0.02728 | 0.77115 |
| 24 | 0.03083 | 0.87146 | 49 | 0.02714 | 0.7671 |
| 25 | 0.03071 | 0.86814 | 50 | 0.02707 | 0.76507 |

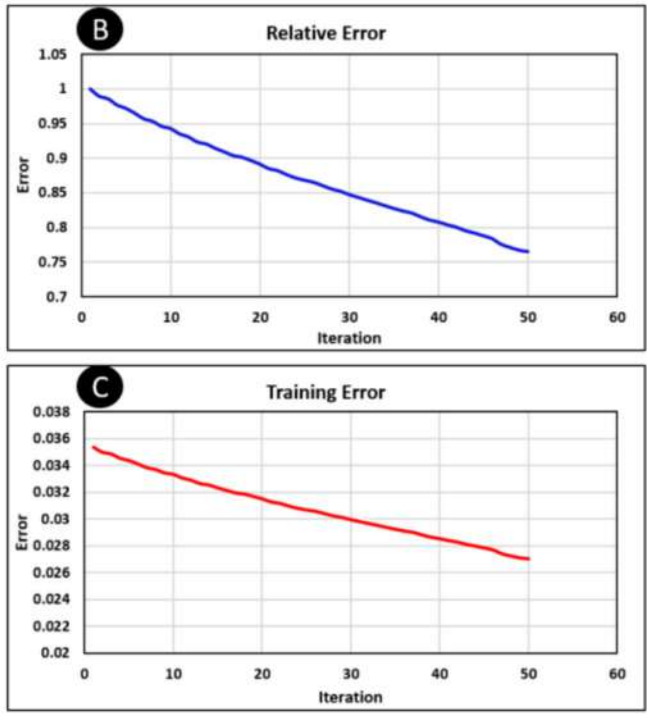


**Fig. 18** **A** Training error table in each iteration, **B** Training Relative error graph, and **C** Training error graph. (In the iteration numbers, the training column reports the neural network error, and the network points error column indicates the relative error)

framework that reveals the complex hydrocarbon architecture within the Bahregansar reservoir and establishes a reliable foundation for optimized field development planning.

## Validation

The validation of lithofacies distribution is relatively straightforward due to the availability of direct well data and established sedimentological principles (Mansouri Siahgoli et al. 2025). In contrast, fluid distribution validation presents significantly greater challenges due to complex factors including dynamic hydrocarbon migration, pressure gradient variations, and multiphase flow behavior (Shahkarami et al. 2014). Effective fluid distribution validation requires sophisticated monitoring approaches, including production data analysis, 4D seismic surveys, and comprehensive reservoir simulation models. Verification is accomplished through direct production testing and indirect validation using reservoir parameters such as fluid contacts and pressure gradients. The PNN method validation in the Bahregansar field demonstrated exceptional accuracy for fluid distribution mapping. Production data from drilled wells completely validated PNN results within the gas area (Ghazban 2007). Although well concentration at the field crest limited oil area validation through production data, both gas and oil probability distributions showed highly acceptable validation through fluid contact parameter analysis. Fluid contact validation through seismic interpretation represents a well-established practice in hydrocarbon exploration (Kumar et al. 2016; Fawad et al. 2020). The integration of seismic attributes with fluid contact analysis proves crucial for reservoir characterization (Chiburis 1984; Proett et al. 2001), with modern multicomponent seismic technologies enhancing determination accuracy using $V_p/V_s$ ratios as reliable fluid indicators (Kumar et al. 2016). Reservoir testing and petrophysical log analysis in the Bahregansar field indicated oil–water contact (OWC) at −2097 m TVDSS and gas-oil contact (GOC) at −2073 m TVDSS. Converting fluid contacts from depth to the time domain and overlaying them

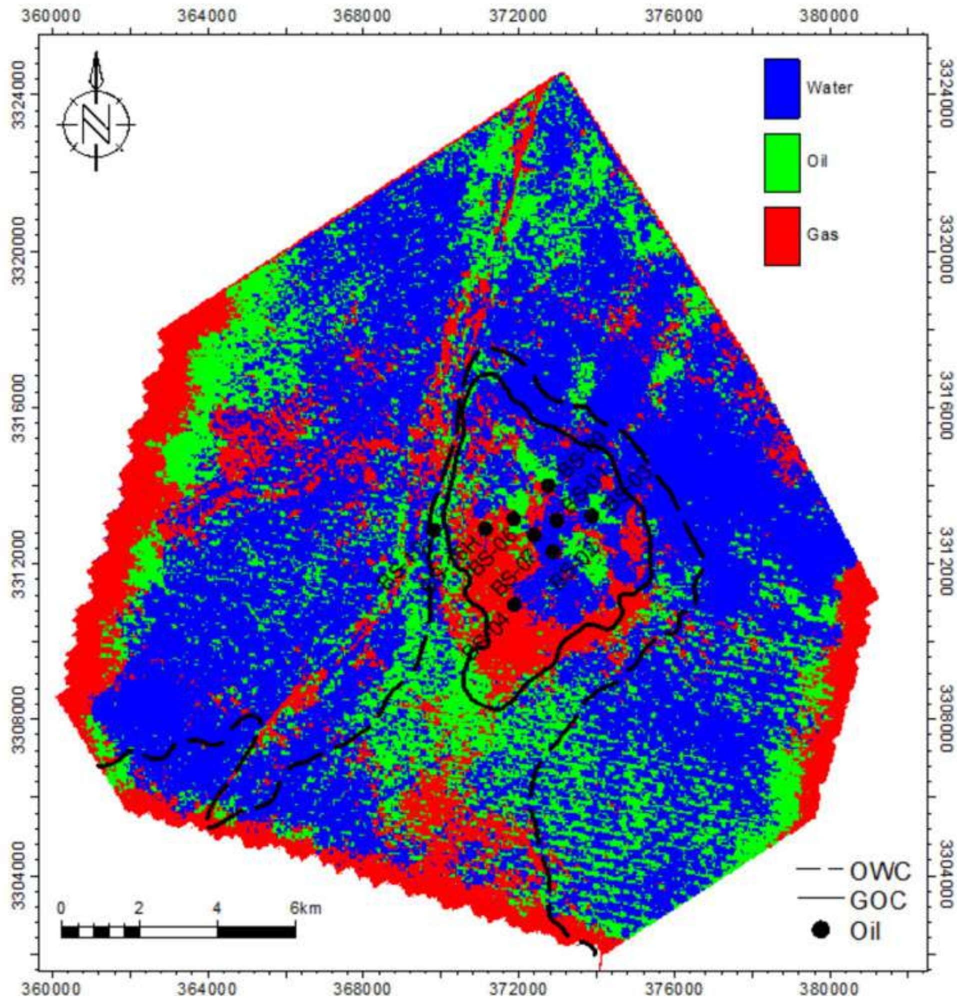


**Fig. 19** The excellent correlation of gas-oil and oil–water contact surfaces (GOC and OWC) with the fluid facies distribution patterns obtained from the PNN method serves as strong validation for the achieved results

on probability distribution maps revealed complete correlation with gas and oil fluid probability distributions. This confirms the PNN method accuracy for exploration predictions and drilling risk reduction (Fig. 19). The validation process achieved remarkably successful results, confirming the integrated approach's effectiveness for fluid distribution mapping.

## Study limitations

Three fundamental constraints affect the interpretation and application of these results:

*Spatial Sampling Heterogeneity*: Well distribution exhibits significant non-uniformity across the field, with concentrations primarily in the structural crest. This heterogeneous sampling pattern introduces potential interpretation bias and reduces result reliability in areas with limited well control.

*Seismic Data Integrity*: Data quality degradation from noise contamination and acquisition footprint effects may compromise AVO indicator accuracy and subsequent interpretative reliability.

*Analytical Scope Constraints*: AVO indicators quantify relative property changes and ratios rather than absolute rock property values. The methodology is inherently limited to two-dimensional map-based analysis and does not provide three-dimensional reservoir characterization. Consequently, both qualitative and quantitative interpretations remain constrained to planar representations.

These limitations emphasize the necessity for integration with complementary datasets and validation methodologies to enhance interpretative confidence and minimize analytical uncertainty in reservoir characterization efforts.

**Acknowledgements** The authors wish to thank the Iranian Offshore Oil Company (IOOC) for their collaboration in conducting this work and for providing access to the data that made this study possible. Special appreciation is extended to Mr. Ali Imandoust, Geoscience Manager at Kish Petroleum Engineering Company (KPE), for his valuable technical support that contributed to improving the results. Finally, the authors gratefully acknowledge KPE for providing the essential software packages used in this research.

**Author contributions** All authors participated in the conceptualization and design of the study. Data collection and analysis were conducted by Hessam Mansouri Siahgoli. The initial draft of the manuscript was prepared by Hessam Mansouri Siahgoli, with subsequent revisions and edits provided by Hessam Mansouri Siahgoli, Mohammad Ali Riahi, Majid Nabi-Bidhendi, and Mohammad Emami Niri.

**Funding** No funding was received for conducting this study.

**Data availability** The data supporting this study's findings are available from the corresponding author upon reasonable request. However, due to privacy or ethical restrictions, the data are not publicly available.

## Declarations

**Competing interests** The authors declare no competing interests.

## References

Agard P et al (2011) Zagros orogeny: a subduction-dominated process. Geol Mag 148(5–6):692–725

Aki and Richards K (1981) 'Aki. K & amp; Richards. P. G. 1980. Quantitative Seismology, Theory and Methods. Volume I: 557 pp., 169 illustrations. Volume II: 373 pp. 116 illustrations. San Francisco: Freeman. Price: Volume I, U.S. $35.00; Volume II, U.S. $35.00. ISBN 0 7167 1058 7', Geological Magazine. 2009/05/01, 118(2), p. 208. Available at: https://doi.org/10.1017/S0016756800034439

Aleardi M (2018) Estimating petrophysical reservoir properties through extended elastic impedance inversion: applications to off-shore and on-shore reflection seismic data. J Geophys Eng 15(5):2079–2090

Alebouyeh M, Chehrazi A (2018) Application of extended elastic impedance (EEI) inversion to reservoir from non-reservoir discrimination of Ghar reservoir in one Iranian oil field within Persian Gulf. J Geophys Eng 15(4):1204–1213

Alvarez P et al (2015) Multiattribute rotation scheme: a tool for reservoir property prediction from seismic inversion attributes. Interpretation 3(4):SAE9–SAE18

Araya-Polo M et al (2018) Deep-learning tomography. Lead Edge 37(1):58–66

Avseth P, Mukerji T, Mavko G (2010) Quantitative seismic interpretation: applying rock physics tools to reduce interpretation risk. Cambridge University Press

Bahroudi A, Talbot CJ (2003) The configuration of the basement beneath the Zagros Basin. J Petroleum Geol 26(3):257–282

Cai F et al (2021) Configuration and timing of collision between Arabia and Eurasia in the Zagros collision zone, Fars, southern Iran. Tectonics 40(8):e2021TC006762

Castagna JP, Swan HW (1997) Principles of AVO crossplotting. Lead Edge 16(4):337–344

Cheng J-W, Zhang F, Li X-Y (2022) Nonlinear amplitude inversion using a hybrid quantum genetic algorithm and the exact zoeppritz equation. Petroleum Sci 19(3):1048–1064

Chiburis EF (1984) Analysis of amplitude versus offset to detect gas/oil contacts in the Arabian Gulf. In: SEG international exposition and annual meeting. SEG, p SEG-1984

Chopra S and Castagna JP (2014) *Avo.* Society of Exploration Geophysicists

Chopra S and Marfurt KJ (2007) Seismic attributes for prospect identification and reservoir characterization. Society of Exploration Geophysicists and European Association of Geoscientists and Engineers

Connolly P (1999) Elastic impedance. Lead Edge 18(4):438–452

Du X et al (2022) Sedimentary and reservoir characteristics of an Oligocene-Miocene mixed siliciclastic-carbonate succession in southeast Iraq. Mar Pet Geol 138:105533

Edgell HS (1996) Salt tectonism in the Persian Gulf basin. Geol Soc Lond Spec Publ 100(1):129–151

Farfour M, Foster D (2022) Detection of hydrocarbon-saturated reservoirs in a challenging geological setting using AVO attributes: a case study from Poseidon field, Offshore Northwest region of Australia. J Appl Geophys 203:104687

Fawad M, Hansen JA, Mondol NH (2020) Seismic-fluid detection-a review. Earth-Sci Rev 210:103347

Feng R (2020) A bayesian approach in machine learning for lithofacies classification and its uncertainty analysis. IEEE Geosci Remote Sens Lett 18(1):18–22

Ghazban F (2007) Petroleum geology of the Persian Gulf. Joint publication, Tehran University Press and National Iranian Oil Company. Tehran University Press

Goodway B, Chen T, Downton J (1997) Improved AVO fluid detection and lithology discrimination using Lamé petrophysical parameters;"λρ","μρ", & "λ/μ fluid stack", from P and S inversions. In: SEG technical program expanded abstracts 1997. Society of Exploration Geophysicists, pp 183–186

Guangjian Z et al (2023) Oil and gas prediction basing on seismic inversion of elastic properties in Chaoshan depression, south China sea. Front Earth Sci 11:1194663

Hampson DP, Schuelke JS, Quirein JA (2001) Use of multiattribute transforms to predict log properties from seismic data. Geophysics 66(1):220–236

Hampson DP, Russell BH, Bankhead B (2005) Simultaneous inversion of pre-stack seismic data. In: SEG technical program expanded abstracts 2005. Society of exploration geophysicists, pp 1633–1637

Johansen TA, Ruud BO, Jakobsen M (2004) Effect of grain scale alignment on seismic anisotropy and reflectivity of shales. Geophys Prospect 52(2):133–149

Khalaf FI, Abdel-Hamid M, Al-Naqi M (2019) Occurrence and genesis of the exposed Oligo-Miocene Ghar Formation in Kuwait, Arabian Gulf. J Afr Earth Sci 152:151–170

Konyuhov AI, Maleki B (2006) The Persian Gulf Basin: geological history, sedimentary formations, and petroleum potential. Lithol Miner Resour 41:344–361

Kumar R et al (2016) A methodology of porosity estimation from inversion of post-stack seismic data. J Nat Gas Sci Eng 28:356–364

Lacombe O et al (2006) Late Cenozoic and modern stress fields in the western Fars (Iran): implications for the tectonic and kinematic evolution of central Zagros. Tectonics. https://doi.org/10.1029/2005TC001831

Ma X-Q (2002) Simultaneous inversion of prestack seismic data for rock properties using a global simulated annealing. Geophysics 67(6):1877–1885

Mansouri Siahgoli H et al (2025) Integrating Bayesian classification and ANN for lithofacies classification using well and seismic data: Bahregansar case study. Disc Appl Sci 7(4):238

Masters T (1995) Advanced algorithms for neural networks: a C++ sourcebook. Wiley

Mohammadrezaei H et al (2020) Deciphering the relationship between basement faulting and two-phase folding in the Hendijan anticline, northwest Persian Gulf, Iran. Mar Pet Geol 122:104626

Mouthereau F, Lacombe O, Vergés J (2012) Building the Zagros collisional orogen: timing, strain distribution and the dynamics of Arabia/Eurasia plate convergence. Tectonophysics 532:27–60

Narayan S et al (2023) Accuracy assessment of various supervised machine learning algorithms in litho-facies classification from seismic data in the Penobscot field, Scotian Basin. Front Earth Sci 11:1150954

Omar GI, Steckler MS (1995) Fission track evidence on the initial rifting of the Red Sea: two pulses, no propagation. Science 270(5240):1341–1344

Orang K et al (2018) Structural framework and tectono-stratigraphic evolution of the eastern Persian Gulf, offshore Iran. Mar Pet Geol 91:89–107

Ostrander WJT (1984) Plane-wave reflection coefficients for gas sands at nonnormal angles of incidence. Geophysics 49(10):1637–1648

Pirouz M et al (2011) Neogene sediments and modern depositional environments of the Zagros foreland basin system. Geol Mag 148(5–6):838–853

Proett MA et al (2001) Multiple factors that influence wireline formation tester pressure measurements and fluid contacts estimates. In: SPE annual technical conference and exhibition. p SPE-71566-MS. https://doi.org/10.2118/71566-MS

Qian F et al (2018) Unsupervised seismic facies analysis via deep convolutional autoencoders. Geophysics 83(3):A39–A43

Russell BH (1988) Introduction to seismic inversion methods. SEG Books

Russell BH, Hedlin KJ (2019) Extended poroelastic impedance. Geophysics 84(2):N1–N14

Russell BH, Lines LR, Hampson DP (2003) Application of the radial basis function neural network to the prediction of log properties from seismic attributes. Explor Geophys 34(2):15–23

Rutherford SR, Williams RH (1989) Amplitude-versus-offset variations in gas sands. Geophysics 54(6):680–688

Sepehr M and Cosgrove JW (2007) The role of major fault zones in controlling the geometry and spatial organization of structures in the Zagros Fold–Thrust Belt

Shahkarami A et al (2014) Artificial Intelligence (AI) Assisted History Matching. In: SPE Western North American and Rocky Mountain Joint Meeting, p. SPE-169507-MS. https://doi.org/10.2118/169507-MS

Sharland PR et al (2004) Arabian plate sequence stratigraphy - revisions to SP2. Geoarabia 9(1):199–214. https://doi.org/10.2113/geoarabia0901199

Smith GC, Gidlow PM (1987) Weighted stacking for rock property estimation and detection of gas. Geophys Prospect 35(9):993–1014

Soleimany B, Sàbat F (2010) Style and age of deformation in the NW Persian Gulf. Petroleum Geosci 16(1):31–39

Song B et al (2023) Direct pre-stack inversion of elastic modulus using the exact Zoeppritz equation and the application in shale reservoir. Front Earth Sci 11:1107068

Specht DF (1990) Probabilistic neural networks. Neural Netw 3(1):109–118

Verm R, Hilterman F (1995) Lithology color-coded seismic sections: the calibration of AVO crossplotting to rock properties. Lead Edge 14(8):847–853

Whitcombe DN (2002a) Elastic impedance normalization. Geophysics 67(1):60–62

Whitcombe DN et al (2002b) Extended elastic impedance for fluid and lithology prediction. Geophysics 67(1):63–67

Zhang C et al (2014) Machine-learning based automated fault detection in seismic traces. In: 76th EAGE conference and exhibition 2014. European Association of Geoscientists & Engineers, pp 1–5